STUDY OF HYDROCARBON PHASE BEHAVIOR UNDER CONFINEMENT EFFECT IN

NANO-SCALE PORES USING LAB-ON-A-CHIP TECHNOLOGY

A Dissertation

by

QI YANG

Submitted to the Office of Graduate and Professional Studies of
Texas A&M University
in partial fulfillment of the requirements for the degree of

DOCTOR OF PHILOSOPHY

Chair of Committee,	Hadi Nasrabadi
Co-Chair of Committee,	Debjyoti Banerjee
Committee Members,	Eduardo Gildin
	Sara Abedi
Head of Department,	Jeff Spath

August 2020

Major Subject: Petroleum Engineering

ABSTRACT

The characterization of phase behavior hydrocarbons trapped in shale reservoir is an enigma and remains a challenging problem due to the phenomenon known as the "confinement effect". This effect is mainly caused by the nano-scale pores which are ubiquitous in shale rocks. The confinement effect becomes increasingly significant in nano-scale pores due to domination of surface-fluid interactions over the bulk fluid-fluid interactions as the size of the pores shrinks progressively. This surface-fluid interaction can lead to anomalous and heterogeneous distribution of hydrocarbon molecules that are confined within the nano-scale capillaries, thereby, resulting in a deviation in the phase behavior of hydrocarbons from its original phase behavior in bulk environment (which is termed as the "confinement effect"). Consequently, several simulation studies reported in the literature were conducted to investigate the confinement effect using the equation of state and density functional theory in molecular simulations by incorporating the effect of capillary pressure in these revised models. However, in the contemporary literature, only a limited number of experiments have been conducted on this topic with the goal of performing experimental validation of the numerical predictions obtained from these simulations, especially for channels with nano-scale dimensions below 10 nm depth and also in high-pressure environments.

In this study lab-on-a-chip technology was explored to quantitatively determine the effect of confinement on the phase behavior of hydrocarbons in nano-scale capillary channels. Initially, the fabrication process of experimental device (which is known as the nanofluidic device) consisting of nano-channels with depths as small as 2 nm was developed and refined (with channel depths

explored in this study ranging from 50 nm to 2 nm and channel widths of 5 microns) . The experimental apparatus was assembled and experimental protocols were developed for performing quantitative measurement of the confinement effect for test fluids (i.e., hydrocarbons). The experimental results involving large capillaries(where confinement effect is trivial) were compared with the phase behavior data (which corresponds to fluids in bulk quantities) for validating the consistency of the experimental protocols. The experimental results show that the confinement effect is exposed and becomes significant for channel depths less than 10 nm. Hence, the confinement effect is more pronounced for smaller capillary size. Specifically, a 23% deviation of dew-point pressure for n-Butane is observed for experimental results involving channels with a nominal depth of 2 nm. Also, hysteresis effects are observed during the experiments involving repeated condensation and evaporation for fluids under confinement. A significant increase in hysteresis effects were observed for channels with a nominal depth of 2 nm (compared to that of deeper channels explored in this study).

DEDICATION

To my parents, Zhongde Yang and Ning Tian for their help, motivation and support.

ACKNOWLEDGEMENTS

I would like to thank chair of my thesis committee Dr. Nasrabadi, Co-Chair Dr. Banerjee and my committee members, Dr. Gildin and Dr. Abedi for their guidance and support throughout the course of this research.

Thanks to staff members at the Texas A&M Materials Characterization Facility (MCF) and the Aggiefab for their support for the fabrication related tasks performed in this study.

Thanks to my colleagues in Dr. Nasrabadi's research group for their assistance with this research.

CONTRIBUTORS AND FUNDING SOURCES

Contributors

This work was supervised by a thesis (or) dissertation committee consisting of Professor Hadi Nasrabadi [advisor] of the Department of Petroleum Engineering (Douglas Von Gonten Faculty Fellow). Professor Debjyoti Banerjee [co-advisor] of the J. Mike Walker '66 Department of Mechanical Engineering (with Joint Courtesy Appointment in Petroleum Engineering Department in the College of Engineering and Department of Medical Education in the College of Medicine; Fellow Engineering Medicine Program; Faculty Fellow in Mary Kay O'Connor Process Safety Center; and Faculty Affiliate in Gas & Fuels Research Center), and Professors Eduardo Gildin (Ted H. Smith '75 and Max R. Vordenbaum '73 DVG Development Professor; Energi Simulation Chair in Robust Reduced Complexity Modeling) and Professor Sara Abedi (C.J. Craft Faculty Fellow) of the Department of Petroleum Engineering.

All experimental work was supported by the Texas A&M Material Characterization Facility and Texas A&M Aggiefab.

Funding Sources

NOMENCLATURE

d_{oxide}	Thickness of the oxide layer
d	Depth of the channel
ε_0	Permittivity of vacuum
ε_{oxide}	Relative dielectric constant of silicon dioxide
E_{eff}	Effective Young's modulus
E_{si}	Young's modulus for silicon
E_g	Young's modulus for glass
h	Channel depth
P_s	Standard saturation pressure
P_{eq}	Equilibrium pressure for capillary condensation with a curved meniscus
R	Universal gas constant
r	Radius of curvature
$V_{applied}$	Voltage used during the bonding process
v_{si}	Poisson's ratio for silicon
v_g	Poisson's ratio for glass
V_m	Molar volume of the liquid
w	Width of the channel
w_{max}	Maximum channel width
γ	Interfacial tension,

TABLE OF CONTENTS

LIST OF FIGURES

LIST OF TABLES

1. INTRODUCTION

1.1 Background

The rapid growth of the of shale oil and gas industry in the United States in the past decade is a direct result of the advancements in production technology, including hydraulic fracturing and horizontal wells. This growth has significantly impacted the United States economy and the dynamics of the international energy markets, which in turn has spurred an increase in research interest along with the deployment of additional resources towards the progressive development of shale oil and gas production. Although production is increasing each year, there is a dire need for its optimization owing to the limited understanding of the dynamics of the fluid flow behavior at different scales within the relevant geological formations.

One substantial difference between the traditional oil and gas industry and the shale oil and gas industry - is that the shale rock system is much more unpredictable and complex in comparison to the traditional system. A reason for this complexity is the presence of nano-scale pores in shale rocks. Pore Size Distribution (PSD) in various shale reservoirs were measured using different methods such as high pressure mercury intrusion [1-3], gas adsorption [1, 4-6], X-ray scattering [1], microscope imaging [7-9] and Nuclear Magnetic Resonance (NMR) [10]. It has been shown that nano-scale pores, especially those smaller than 10 nm, can occupy up to 40% of the total pore volume in a shale system [10].

The hydrocarbons present in nano-scale pores, in comparison to those present in bulk, exhibit different physical behavior. This altered physical behavior is caused by the fluid–wall interaction in addition to the fluid–fluid interaction. The closer the size of the hydrocarbon molecules to the

1

size of the space they are confined in, the more pronounced the fluid–wall interactions. As a result, this leads to more significant physical behavior alterations. These alterations in behavior include both: (a) new types of phase transitions, and (b) shifts in phase transitions. The new types of phase transition not observed in a bulk environment include layering [11, 12], wetting [13, 14] and commensurate–incommensurate transitions[15-17], etc. The shifts in transition includes change of phase transition temperature and pressure in gas-liquid, liquid-solid or liquid-liquid phase transitions etc.

A comprehensive understanding of confined fluid behavior is crucial for many research areas such as biotechnology, medicine [18-22] and water purification [23, 24]. Micro- and meso-pores (pore width of sub-2 nm and 2-50 nm, respectively) are widely present in industrial processes related to these research areas, including the pharmaceutical industry, chemical industry, and food industry. The designs of such processes are largely experience-based at the moment and require more scientific knowledge—this is also true of the shale oil and gas industry. One of the problems currently facing the industry is devising mechanisms to accurately predict the hydrocarbon fluid-phase behavior in shale systems. The pressure–volume–temperature (PVT) properties in shale systems are different from those in a bulk environment. This phenomenon is known as the confinement effect [25, 26]. A better understanding of this confinement effect could result in substantial improvement in the process of enhanced oil and gas recovery (EOR) [27-31].

Several researchers have applied various simulation methods to study confined-phase behavior. For instance, the equation of state (EOS) along with the capillary pressure, which is calculated using the Young–Laplace equation for nano-scale pores, has been widely used to predict the

confinement effect [29, 32-34]. However, this method fails to account for the fluid–surface interactions, which occur when the nano-capillary size is below 10 nm and the size of the molecule is comparable to the space it is confined in [35]. In addition, some studies have reported the application of modified critical properties of the pure components, which were calculated from molecular simulations to generate the phase envelop of hydrocarbon fluids using EOS [36-39]. Moreover, density functional theory has also been applied in combination with EOS to investigate the adsorption and phase behavior of the hydrocarbon fluids [40, 41].

Another important way of predicting hydrocarbon phase behavior in a confined environment is through molecular simulations. Molecular simulation techniques such as Grand Canonical Monte Carlo (GCMC) and Gibbs Ensemble Monte Carlo (GEMC) are used to understand the phase behavior under the confinement effect [42-49]. Molecular simulation with the statistical thermodynamic approach is a powerful tool to simulate the scenarios with heterogeneous molecular distributions, which is the case for hydrocarbon molecules in nano-scale capillaries. This method has demonstrated the properties of being highly customizable and versatile with the downside of sometimes being time consuming.

Very few experimental validations have been reported in the literature while a large volume of literature reports involved numerical predictions of confinement effect. This dearth in experimental reports could be attributed to the technical difficulties in obtaining porous samples that can represent shale rocks and the challenges in performing the experiments. The traditional PVT characterization method include the use of PVT cells, optical method, electrical method and acoustic method [50]. PVT cell phase behavior experiments are usually performed by utilizing

various types of reservoir fluids for conventional reservoirs. However, these techniques fail to account for nano-scale pores, such as those in shale rocks which traps hydrocarbons. Further, these experiments are time consuming and costly in comparison to other methods. Methods for characterizing traditional fluid phase behavior include cooled mirror method [51], absorption spectroscopy [52]and fiber-optic reflectometer methods [53, 54] etc.

As mentioned before, only a few studies have conducted hydrocarbon phase behavior experiments in the nano-scale pore environments. Luo et al., for instance, recently applied the Differential Scanning Calorimetric (DSC) technique to measure the bubble-point temperature shift of both pure hydrocarbons and mixtures under the confinement effect [55-58]. The DSC technique investigated the thermal properties of the sample by measuring the heat flow of the sample during a controlled temperature increase. During the phase transition, as per theory, the amount of heat required to keep the same rate of temperature increase in the sample will change and this change will be detected as the phase transition temperature. In these experiments, glass particles with pores ranging from 4.1 nm to 38.1 nm in diameter on their surface were merged with hydrocarbons and placed in a container as the sample. The temperature of the sample was increased at a steady rate and the phase transition temperature was recorded upon the detection of changes in heat flow. An increase in the bubble-point temperate was observed for both pure hydrocarbons and their mixtures under confinement. However, this approach lacked direct observation of the hydrocarbon phase change and was limited to low pressure environment.

Another study performed an isochoric experiment with synthesized porous media made by using barium titanate particles to measure the dew-point condition of a gas mixture of ethane and pentane

[59]. A packed bed of by barium titanate, with pores with diameters ranging from 5 nm to 50 nm, was saturated with a hydrocarbon mixture and placed in an isochoric apparatus. The pressure was monitored for a fixed volume of fluid, that underwent an isochoric process under the confinement effect and in a bulk environment at the same time. The results were plotted on a pressure versus temperature plot and the point of slope change was recorded as the phase transition point. The results showed an increase in dew-point pressure for the mixture at around 240 °F owing to the confinement effect. However, this method, owing to the nature of the sample, failed to characterize the pore size distribution of the sample and thus demonstrated potential problems for simulations to reproduce its results.

Recently, the lab-on-a-chip technology has been applied to study the confinement effect. This concept involves conducting experiments in a miniaturized micro/nano-fluidic device instead of a laboratory. Lab-on-a-chip technology has been widely used in several research areas such as water desalinization [23, 24, 60, 61], drug delivery [62-65] and analytical chemistry [66-68]. For the oil and gas industry, lab-on-a-chip technology has been used with microfluidic device for many research purposes such as traditional PVT measurements and phase envelop generation [69-76], solubility measurements [77-80], diffusivity measurements [81-84], miscibility measurements [85] and precipitation measurements [64, 86-90]. It has several advantages over other methods in phase behavior studies. Firstly, this technology is more economical than other methods. Since the pore volume in nanofluidic devices is extremely small, the required amount of hydrocarbons, which can be very expensive if reservoir fluid is used, is small. Secondly, this technology can also be very time efficient. A typical experiment session usually takes 4 to 5 hours from preparation to finish while other methods may take days to accomplish the same task. Thirdly, the device is highly

5

customizable. With well-developed fabrication process, the nanofluidic device can achieve a depth as low as 2 nm with a 10% tolerance [91]. Further, different types of geometries can be fabricated involving different morphologies of nano-capillaries. These can be typically designed and developed using a photomask. An optically transparent glass wafer can be bonded on top of the silicon wafer (containing micro-scale and nano-scale capillaries). This facilitates visual access for observing the phase transition behavior of the confined fluids (such as hydrocarbons) in these experiments under different pressure and temperature conditions.

Several researchers have conducted hydrocarbon phase behavior experiments with lab-on-a-chip technology using nanofluidic device [50, 69, 72, 92-99]. Wang et al. measured the bubble-point temperature of a ternary mixture of n-Octane, n-Butane and i-Butane with a nanofluidic device containing 100 nm deep channels. In the experiments, an increase in bubble-point temperature was observed for the injected fluid [92]. Parsa et al. measured the condensation pressure of propane in 500 nm, 50 nm and 30 nm channels, wherein a minimal decrease in dew-point pressure was observed in 30 nm channels and no significant change in dew-point pressure was observed in 50 nm and 500 nm channels [93]. In addition, Alfi et al. investigated the confinement effect on the bubble-point temperates of hexane, heptane and octane in 50 nm channels; however, no significant confinement effect is detected [94]. It is important to note that the studies mentioned above used nano-capillaries with a depth greater than 30 nm, which, in fact, is not small enough to detect the confinement effect and to represent the nano-scale pores in shale rock. Currently, to the best of our knowledge, only one study has performed experiments using a sub-10 nm nanofluidic device, which was conducted by Zhong et al [95]. In the study, a nanofluidic device with channel size of 8 nm was used to measure the condensation temperature of propane. The temperature was

6

controlled by a water bath and measured using a built-in thermocouple. An increase in condensation temperature was observed in 8 nm capillaries.

In this work, nanofluidic devices containing nanochannels with depth ranging from 50 nm to 2 nm have been fabricated. Further, a high-pressure experimental setup has been built. The fluid confinement effect for the phase behavior of various hydrocarbons is investigated. The methodology is validated by first conducting the experiment in capillaries with nominal depth of 50 nm (which are expected to demonstrate negligible confinement effect). Significant confinement effects are observed in capillaries with depths of 10 nm, 4 nm and 2 nm. In addition, anomalous behavior is observed in these experiments where hysteresis in phase transition occurred for fluids confined in channels with nominal depths of 50 nm; these hysteresis effects are more pronounced for channel depths lower than 10 nm. High pressure experiments have also been conducted for n-Butane 10 nm channels. The effect of temperature on confinement is evaluated at various temperatures. It is observed that the confinement effect is less pronounced at higher temperatures.

2. METHODS[*]

2.1 Nanofluidic Device Design and Fabrication

2.1.1 Device Design

Lab-on-a-chip technology provides multiple levels of flexibility in the design of the nanofluidic devices. The complexity of the design paradigms and architecture can vary from a single channel to a network of channels. Also, the flexibility in the plethora of the robust fabrication processes that are available for deployment enables different channel depths within the same device. The depth of the channel can vary from several microns to as low as 2 nm. This enables a more realistic design to be implemented that mimics the shale rock matrix with fractures. Figure 1 showcases some patterns that have been designed or fabricated.

In this work, two types of nanofluidic devices were utilized in the experiments. The first type was fabricated by bonding two layers of glass chip, with the bottom substrate containing nano-capillaries. The second type was fabricated by bonding a silica wafer to a glass layer, with the silica wafer containing etched nano-channels. The earlier model was directly purchased from Klearia, and the latter model was fabricated in Aggiefab.

The first type of experimental platform was obtained after bonding rectangular shaped substrates (with dimensions of 41.1 mm by 25.4 mm by 2 mm). Several designs of the geometry of the capillary channels were produced and utilized to perform experiments. After trial and error, the nanofluidic platform consisting of 3 single parallel channels was chosen as the final design (as

---

[*] Part of the data reported in this chapter is reprinted with permission from "Direct visualization and molecular simulation of dewpoint pressure of a confined fluid in sub-10 nm slit pores" by Yang, Q., Jin, B., Banerjee, D., & Nasrabadi, H., 2019. *Fuel, 235*, 1216-1223. Copyright [2018] by Elsevier Ltd.

shown in Figure 2). The channels were designed to originate from a cylindrical reservoir. The width of the channels was fixed for a uniform value of 5 μm and the depth of the channel was varied from 50 nm to 2 nm. In this work, the experiments were performed for nominal values of channel depth of 50 nm, 10 nm, 4 nm, and 2 nm.
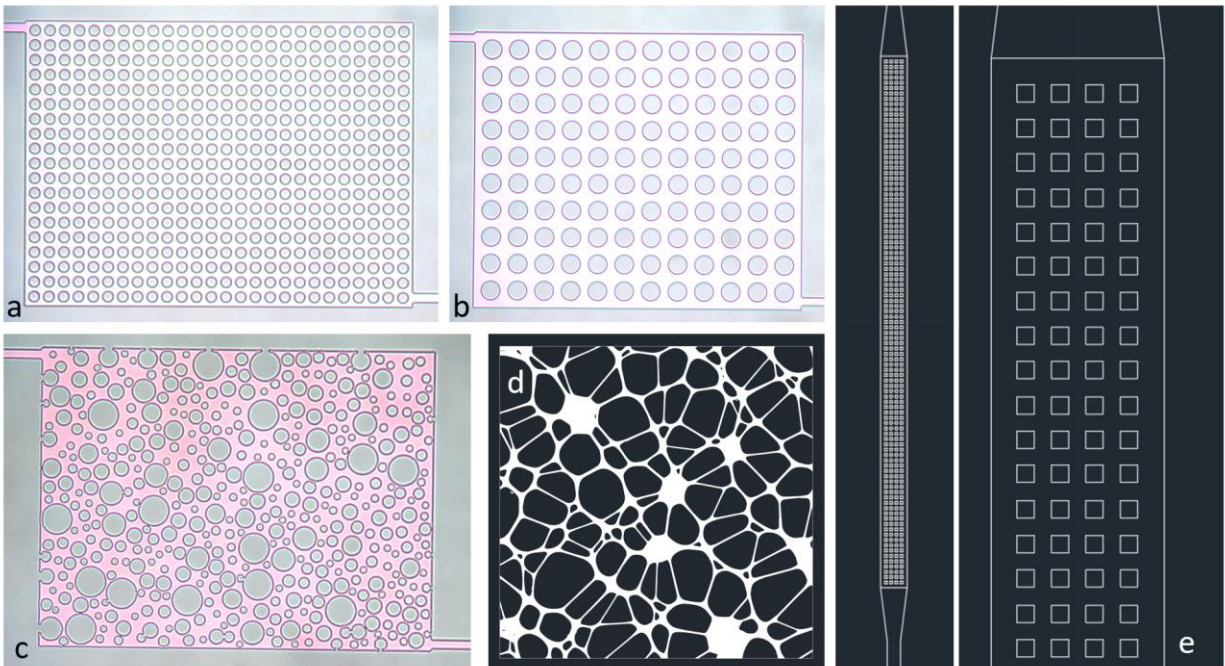
Figure 1. Pattern design of the nanofluidic device. (a, b) Images of fabricated microstructures (top view) in channels with symmetric and regular patterns. (c) Image of a microchannel (top view) with an irregular pattern of microstructures. (d) AutoCAD design of a pattern that mimics rock matrix. (e) A simplified design to mimic the shale matrix with fracture. The deeper channel (top and bottom part) is connected to the shallower channel (middle part) with rectangular pillars in the middle.
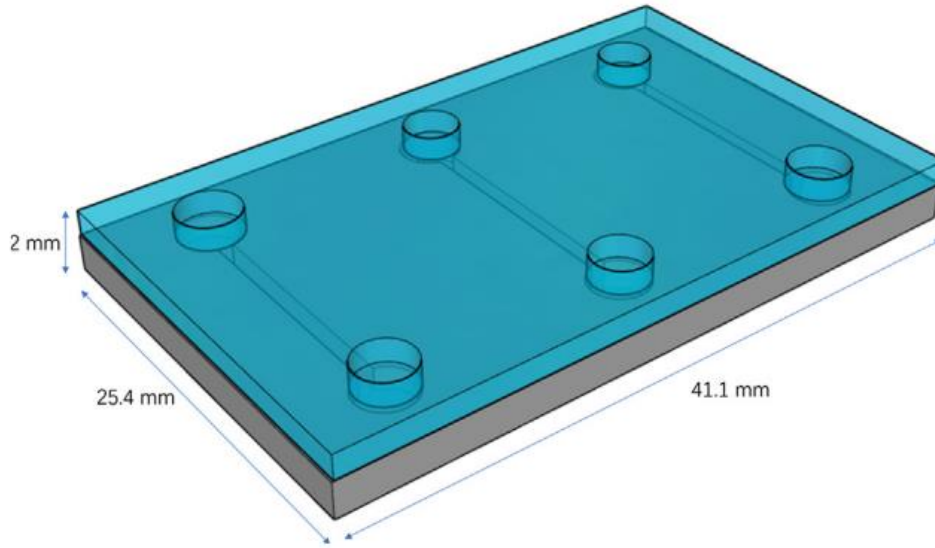
Figure 2. Schematic of the nanofluidic device. Nanofluidic device was made by bonding the bottom layer (containing etched nano-channels) with the top cover layer containing through holes for providing fluidic access (i.e., using fluidic connector ports that were mounted subsequently on these through holes).

The second type of experimental platform was obtained after bonding circular-shaped substrates (or wafers) with a radius of 4 inches and a thickness of 0.5 mm (or 2 mm), where the thickness of the wafer depends on the thickness of the glass layer used during micro/nano-fabrication processes. The thinner glass wafer with a thickness of 0.5 mm is suited for conducting low-pressure experiments and the thicker glass wafer is suited for conducting high-pressure experiments. The pressure tolerance testing data for these devices is demonstrated in the results section. The patterns on the second type of experimental platform are more diverse, ranging from single channels to a network of channels. Figure 3 showcases some of the devices.
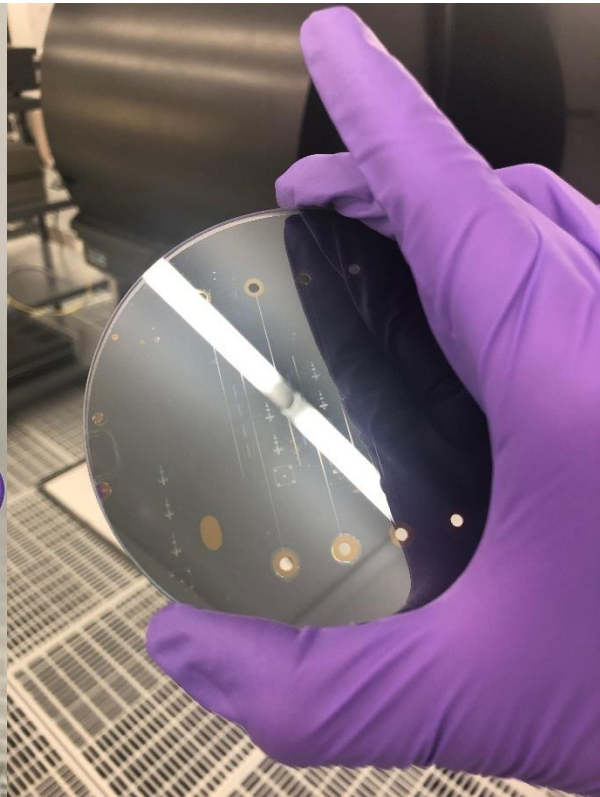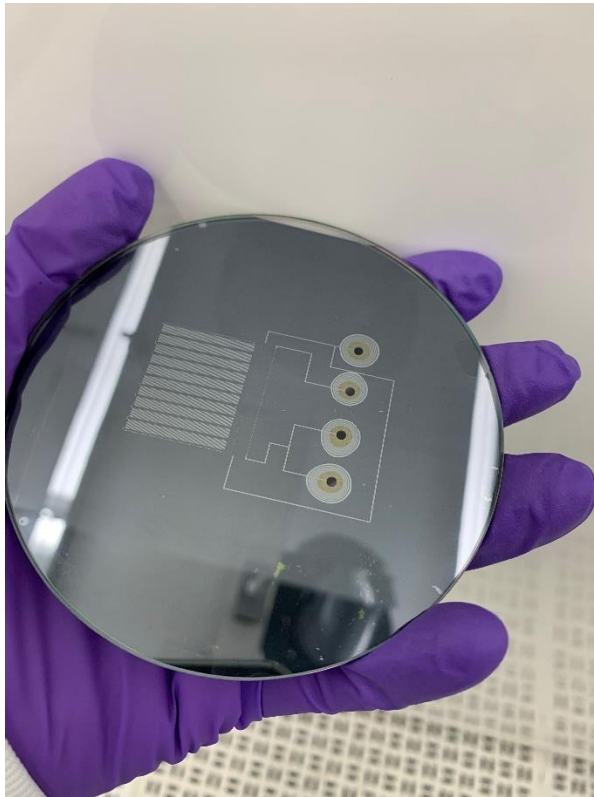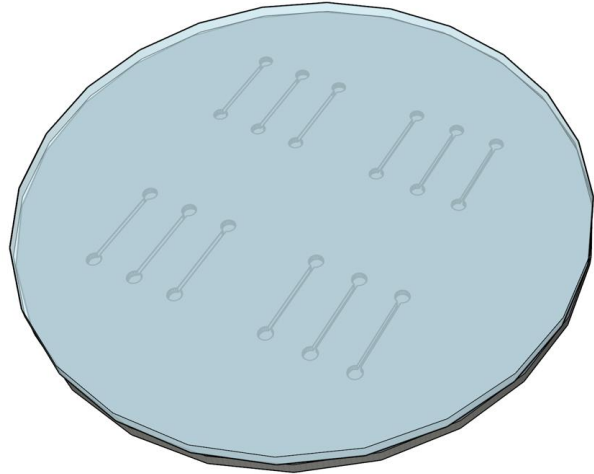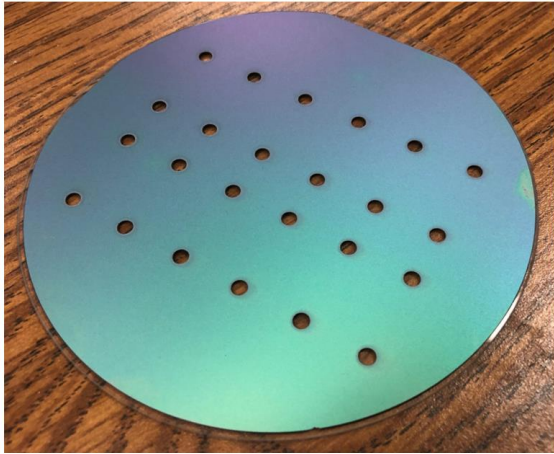
Figure 3. Circular wafer with nanofluidic device. Nanofluidic device was made by bonding the silica wafer (containing with nano-channels) in the bottom with the glass wafer on top.

The designs of these device are chosen based on a few criteria. For low-pressure experiments, the footprint of the nanofluidic device needs to fit under a microscope. For high-pressure experiments,

the footprint of the nanofluidic device needs to fit into a stainless-steel manifold. The manifold is designed to contain the nanofluidic device for conducting the high-pressure experiments safely. The manifold, along with the device, is placed under a microscope for visual observations during the performance of the experiments.

For pattern design, one limitation is that the minimum feature size needs to be 1 µm. This limitation is not only because of visualization purposes under a microscope, as small features are challenging to observe, but also because of the fabrication technique chosen in this work, which will be discussed in the later sections. Besides this limitation, a simpler design, for example a single channel, increases the probability of success for conducting the experiments. Therefore, even though many designs of the device were fabricated, for measuring hydrocarbon phase behavior in extremely small nano-capillaries, most experiments, in this work, are conducted in single channels. More intricate designs can certainly be utilized as they can better mimic the shale matrix, as will be discussed in the future work section of this thesis.

One thing to mention is that the aspect ratio (channel width vs. channel depth) needs to be taken into consideration for the design of extremely shallow channels. Ensuring the stability and structural integrity of the channels pose some of the biggest challenges when fabricating the nanofluidic devices, especially during the final bonding process. A channel that is too wide for a given depth has a very high chance of collapsing during the bonding process and can lead to catastrophic failure. A few parameters need to be taken into consideration when it comes to the stability of the channel during the bonding process. These parameters include the temperature and voltage used during the bonding process. The thickness of the oxide layer and the aspect ratio of

the designed channel. According to the model established by Duan and Majumdar [91], the maximum width of the channel that can be fabricated without channel collapsing during the bonding process can be calculated as follows:

$$w_{max} = \frac{E_{eff} d_{oxide}^2 h}{\varepsilon_0 V_{applied}^2 \varepsilon_{oxide}^2} \qquad (1)$$

where, w_{max} is the maximum channel width, d_{oxide} is the thickness of the oxide layer, h is the channel depth, ε_0 is the permittivity of vacuum, $V_{applied}$ is the voltage used during the bonding process, ε_{oxide} is the relative dielectric constant of silicon dioxide and E_{eff} is the effective Young's modulus defined by equation:

$$\frac{1}{E_{eff}} = \frac{(1-v_{si}^2)}{E_{si}} + \frac{(1-v_g^2)}{E_g} \qquad (2)$$

where, v_{si} and v_g are the Poisson's ratio for silicon and glass, and E_{si} and E_g are the Young's modulus for silicon and glass at the bonding temperature respectively.

For a silicon wafer with a 500 nm silicon dioxide layer that is bonded to a glass layer maintained at 400 °C and subjected to 600 V, containing channel with a depth of 2 nm, this model predicts that the maximum channel width is limited to a maximum value of 2 µm in order to prevent the collapse of the capping wafer into the channel during the bonding process. However, for channels that are 4 nm in depth (or larger), the typical channel width of 5 µm is used.

In this study, glass wafers with thickness of 0.5 mm and 2 mm were used. The thicker glass wafer was chosen to afford higher-pressure tolerance. In order to have a successful bond, the voltage and temperature need to be high enough. Table 1 provides the recommended temperature and voltage parameters depending on the type of the glass wafer used for glass-silicon anodic bonding [100]:

Table 1. Quality of glass to silicon wafer anodic bonding. Quality with various thickness, temperature and voltage [100].

Type of glass	Thickness [mm]	Temperature [°C]	Voltage [V]					
			500	700	900	1000	1200	1500
Borofloat 33	1	250	A	A	A	A	A	A
		300	A	A/B	A/B	B	B	B
		350	A	B	B/C	B/C	C	C
		400	B	B/C	C	C	C/D	D
		450	B	C	D	D	D	D
	2	300	A	A	A	A	A	A
		350	A	A	A/B	A/B	B	B
		400	A	A	B	B	B/C	C
		450	A/B	B	B/C	C	C/D	D

Here A, B, C and D represents bonding quality with A being the poorest quality and D being the best quality. According to the table's recommendation, the bonding parameters for 2 mm glass layers need to be 400 ℃ and at least 1200 V in order to achieve a C or D tier bonding. With these parameters, the calculated w_{max} is about 0.6 µm which is smaller than the minimum requirements for the design. Therefore, there is a tradeoff between a device's ability to tolerate high pressure and the device's ability to hold extremely shallow channels, especially for channels that are around 2 nm in depth. A higher temperature and imposed voltage during the anodic bonding process could

reduce the maximum width of the channel by a big margin and thus limiting the design options (as well as applicability for different experimental platforms). One possible way to mitigate this constraint is by increasing the oxide layer thickness. According to the model, w_{max} is proportional to the square of the thickness of the silicon dioxide layer. All current devices have a silicon dioxide layer of 500 nm thickness. In theory, an oxide layer of 1 µm could prevent a channel of 2.4 µm in width and 2 nm in depth from collapsing with the 2 mm thick glass. However, the device with 1 µm oxide layer was not fabricated in this study.

2.1.2 Device Fabrication

The second type of experimental platforms (the circular device with silicon wafers) were fabricated on campus at Texas A&M University (using shared user facilities available at Aggiefab). The nanofluidic device fabrication process was adapted from semiconductor manufacturing processes (and these techniques have also been translated to research studies in other disciplines such as in chemistry and biomedical engineering). However, in this study, these fabrication procedures were modified and attuned for meeting the experimental requirements while also maximizing the multiplexing (i.e., number of channels) on these experimental devices.

Prime grade silica wafers were procured commercially from University-wafer (City, State) and chrome masks were sourced commercially using the Photomask Portal (City, State). For the silicon wafers, the first step is to generate a layer of silicon dioxide on a silicon wafer substrate using dry/ wet oxidation or Plasma-Enhanced Chemical Vapor Deposition (PECVD). The dry/wet oxidation procedure is performed using MINIBRUTE Oxidation Furnace, and the PECVD is performed using Oxford Plasmalab80Plus (located in Aggiefab). The thickness of oxide layers was measured

using Ocean Optics NanoCalc DUV Spectroscopic Thin Film Measurement tool which afforded a resolution of 0.1nm. The dry/wet oxidation process affords both advantages and suffers from disadvantages (when compared to PECVD process). The dry/wet oxidation process is used to oxidize the surface of the silica substrate wafer and obtain a thin-film of silicon dioxide (silica). This is accomplished by heating the substrate to steady state temperature conditions followed by blowing oxygen and water vapor onto the substrate surface (in the dry oxidation process, only oxygen is used). The rate of oxidization depends on the temperature of the furnace, the concentration of oxygen and the duration of the oxidation process. This method produces oxide thin films with an extremely low surface roughness, which is perfect for etching shallower channels such as channels shallower than 10 nm. However this method is very slow and is time consuming (requiring about 90 minutes to generate an oxide layer of 500 nm thickness for wet oxidation while requiring 35 hours for dry oxidation at 1000 °C). This can also result in non-uniformity of the thickness of the oxide thin film across a wafer, especially for thicker films due to the non-uniformity in the oxygen concentration and flow distributions during oxidation. However, the non-uniformity of film thickness was not important in this study as the film thickness in this study was limited to the range of 100 ~ 200 nm. PECVD, on the other hand, is a much faster and simpler process from an operational viewpoint. This process affords the generation of thin films with better uniformity in the thickness values. However, for the thin films generated in this study, the Atomic Force Microscopy (AFM) measurements showed that the surface roughness of the wafers was in the range of 10 nm. Therefore, this will not be appropriate for the shallower channel fabrication required in this study. However, for deeper channels, this can be a feasible option. The devices fabricated in this study with sub-10 nm channels employed primarily dry/wet oxidation process.

In this study, the standard photolithography technique is adopted for imprinting microscale patterns of the width of the nanochannels on the silicon wafers. The photolithography process affords multiple advantages compared to that of other methods, such as electron beam lithography (EBL) [101-103] and porous silicon etching [104-106]. After generating a silicon dioxide layer, a layer of photoresist AZ4214e is spin-coated on the silicon dioxide layer by mounting the silicon wafer on a spin coater. The wafer is placed onto the spin coater with drops of photoresist liquid on top. Following which, at 4000 rotations per minute (RPM) for 45 seconds to form a uniform layer of photoresist. This spin speed is chosen based on the manufacturer specification (of the photoresist) in order to obtain a photoresist thickness of 1 µm, which is deemed appropriate for the photolithography step. The photoresist acts as a barrier (protection layer) for the subsequent etching process. Following the spin coating, the wafer is soft baked on a hot plate at 90 °C for 2 minutes.

After spin-coating and soft-baking the photoresist, a photomask with a designed channel pattern is aligned on the top of the wafer using EVG 610 Double-sided Mask Aligner. A photolithography process is then executed by exposing the mask and photoresist using UV light. This alters the solubility of the exposed photoresist. The exposure dose correlates to the photoresist film thickness, which, in this case, is 100 mJ/cm^2. A lower dose could cause photoresist to be underdeveloped and block the silica underneath from etching. Excess optical dose could cause photoresist to be overdeveloped and can ruin the desired pattern. Also, the optical resolution of the chosen photolithography process is limited to a minimum value of 1 µm. Hence, feature dimensions (critical dimension/ CD) smaller than 1 µm risk not being developed appropriately.

Since the exposed photoresist is soluble, it is dissolved using a developer solution (AZ 726), thereby exposing the silicon dioxide underneath. The part of the photoresist that is covered by the features in the mask (during photolithography process) remains unaffected during this process. After developing, the wafer is hard-baked on a hot plate at 135 °C for 8 minutes.

After photolithography and developing process, the wafer is dry etched by the Reactive Ion Etching (RIE) process using Oxford Plasmalab 100 ICP RIE to form the capillary channels with the desired depth and width. The dry etching process parameters are designed to etch the exposed silicon dioxide thin films at a faster rate than the photoresist and the silicon wafer. The etching speed can be controlled by modulating several process parameters such as the gas flow rate and the chamber pressure. In this study, at a room temperature of 20 °C , the imposed radio frequency (RF) power is set at 150 W, with an oxygen flow rate of 5 sccm and CHF_3 flow rate of 45 sccm - are used for the etching process. Multiple devices are fabricated by varying the duration of the etching process. By interpolating the measured value of the etch depth obtained from AFM (Figure 4) as a function of the etch duration, it was concluded that the etch rate corresponding to these process parameters for silicon dioxide is about 0.5 nm/ second.
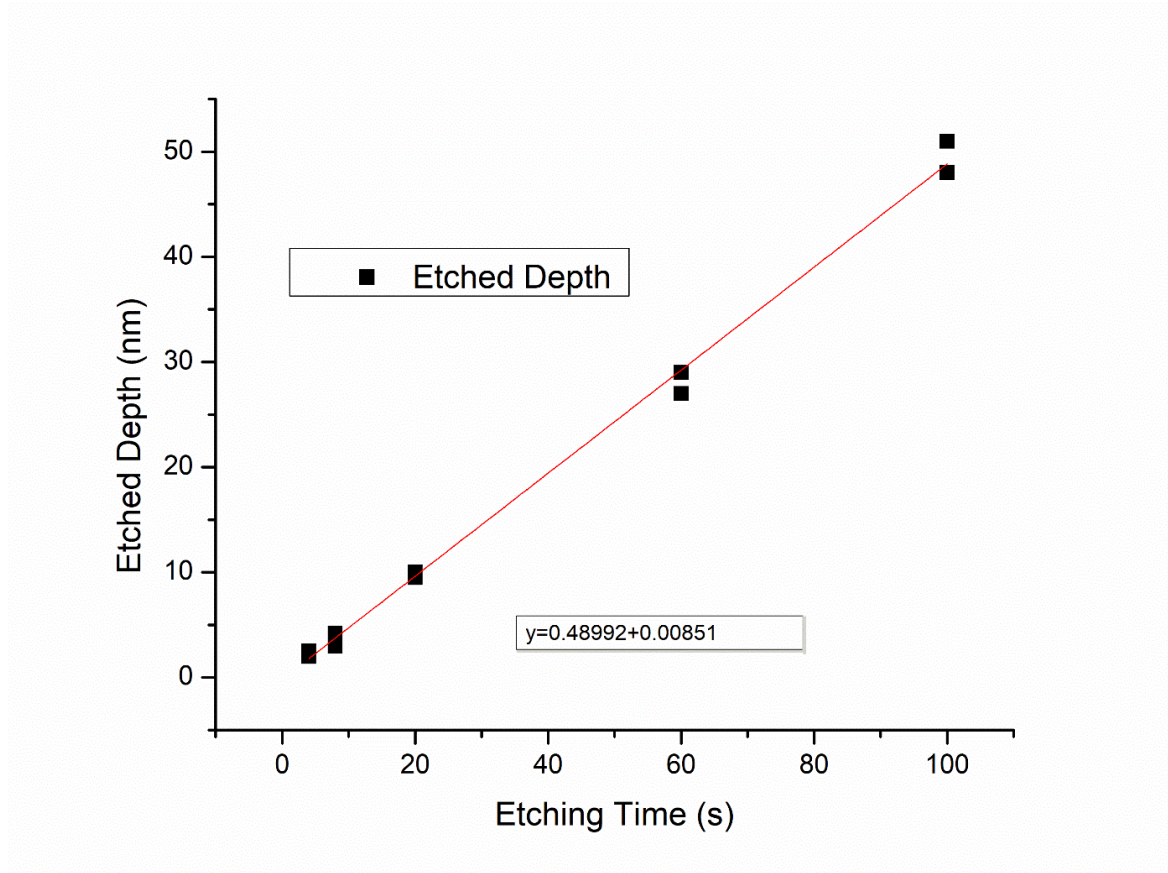
Figure 4. Fabricated channel depth vs. etched time.

After the etching process, the remaining photoresist is removed by immersing the wafers into AZ400T stripper that is heated to a temperature of 90 °C . Due to the hardened photoresist, this step takes from half an hour to several hours to finish. After the photoresist is removed, the depth of the channel is checked again using Bruker DektakXT Surface Profiler, especially for measuring channels with larger channel depth. For shallower channels, the channels are characterized by using AFM since this technique can afford a resolution of channel depths to about 0.1 nm.

If the device design requires the fabrication of channels with multiple depths, the same process steps are repeated for the channels with larger values of channel depths after fabricating the

channels with a shallower channel depth (i.e., from coating photoresist onto the wafer to the feature characterization, are repeated). The mask alignment is performed carefully during the photolithography process to ensure that the features developed in the second round are properly aligned (and connected) to the features that have already been developed in the previous steps. The shallow features are etched initially for affording better quality of all of the features and improving the yield of the process steps. The wafers are then shipped to Questech Services Corporation for leaser drilling of the through holes. The through holes also act as reservoirs in addition to providing access for fluidic connections to the fabricated channels.

In the last step, each wafer is bonded to a glass slide by anodic bonding using EVG 501 Wafer Bonder to complete the nanofluidic device fabrication process. Two types of glass slides are used in this study. The first type is 500 µm thick and the second type is 2 mm thick. Depending on the glass wafer chosen for this study, the anodic bonding process varies. For a 500 µm thick glass a voltage of 600V is used and the hotplate is set at 400 °C. For a 2 mm thick glass wafer a voltage of 1200V is used and the hotplate is set at 400 °C . This recipe is observed to provide the best yield. A schematic of the fabrication procedure is shown in Figure 5.
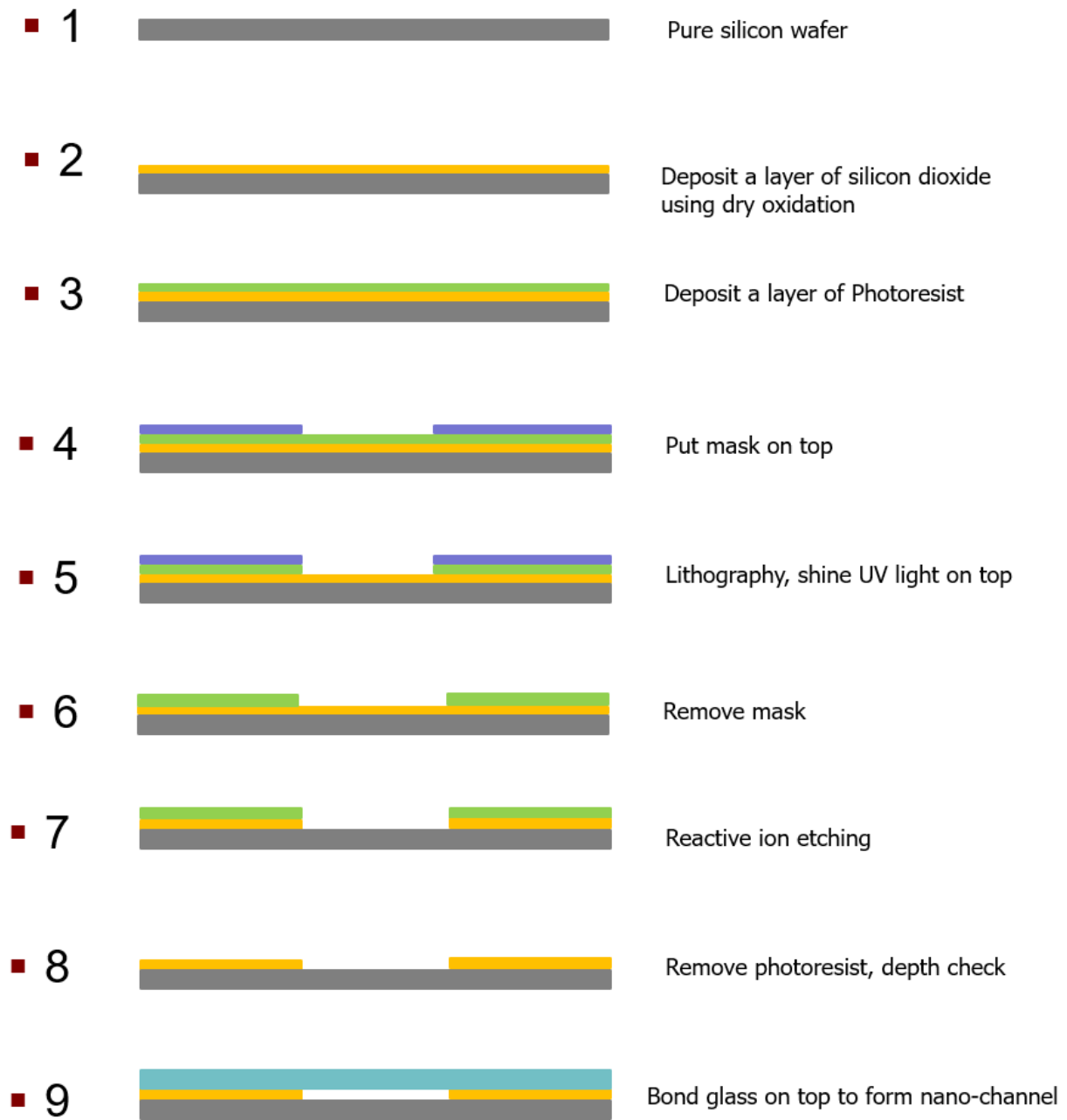
Figure 5. Schematic of the fabrication process for the nanofluidic device.

2.2 Experimental Setup

Two different experimental setups were designed, fabricated and assembled for this study. The first experimental setup was designed for operation at low-pressures, is simpler and easier to operate. This experimental setup was designed to demonstrate feasibility of the proposed approach at low-pressures and also to validate the experimental methodology. The latter experimental setup required more sophisticated experimental approach, and in theory, can achieve a pressure rating of more than 7000 psi. Also, the latter experimental setup provides a better fluid flow and imaging capabilities.

In this work, n-Butane was selected as a working fluid in order to serve as a pure component for the dew-point pressure measurements. It may be noted that n-Butane in bulk quantities has a dew-point pressure of around 35 psia under room temperature conditions [107], which is a relatively easy experimental condition to implement.

2.2.1 Low-pressure Setup

For low-pressure experiments, a gas cylinder containing n-Butane (Matheson Gas, G1905075-LB), with 99.9% purity, is used as the test fluid for these experiments. To ensure safety, a dual stage pressure regulator is attached to the gas cylinder to control the pressure (Matheson Gas, 3850-170 CGA). A hand pump (Martel Electronics, MECP 10 K) is used to pressurize the n-Butane gas by squeezing deionized (DI) water into the connected tubing. A high accuracy pressure gauge with an error of 0.05% (Martel Electronics, The BetaGauge PI PRO) is attached on top of the pump to acquire pressure measurements. A three-way valve (IDEX Health & Science, V101-L) is applied to switch the connection from the nanofluidic device to either the gas cylinder or the

hand pump. A vacuum syringe is used to apply a pressure drop to accelerate hydrocarbon flow in the nano-capillaries. High pressure resistant tubing (IDEX Health & Science, 1500) and nano-ports (IDEX Health & Science, N-333) are used to connect all the devices together. Finally, Teflon tape is applied to all joints to ensure a pressure-sealed environment. The experimental set up is shown in the Figure 6. The chip is placed under a microscope (Olympus America, Olympus IX-81) equipped with UPLSAPO 20X/0.75 objective and a Rolera XD CCD camera for direct observation of the hydrocarbon phase change. A 488 nm laser is chosen for illuminating the nano-channels. Due to the potential temperature increase caused by the laser source and the high temperature sensitivity of n-Butane dew-point pressure, an Infrared (IR) camera (FLIR 150) is used to accurately monitor the temperature of the devices and apparatus during the experiments (a schematic of the experimental apparatus is shown in Figure 6 and a sample of the infrared image is shown in Figure 7).
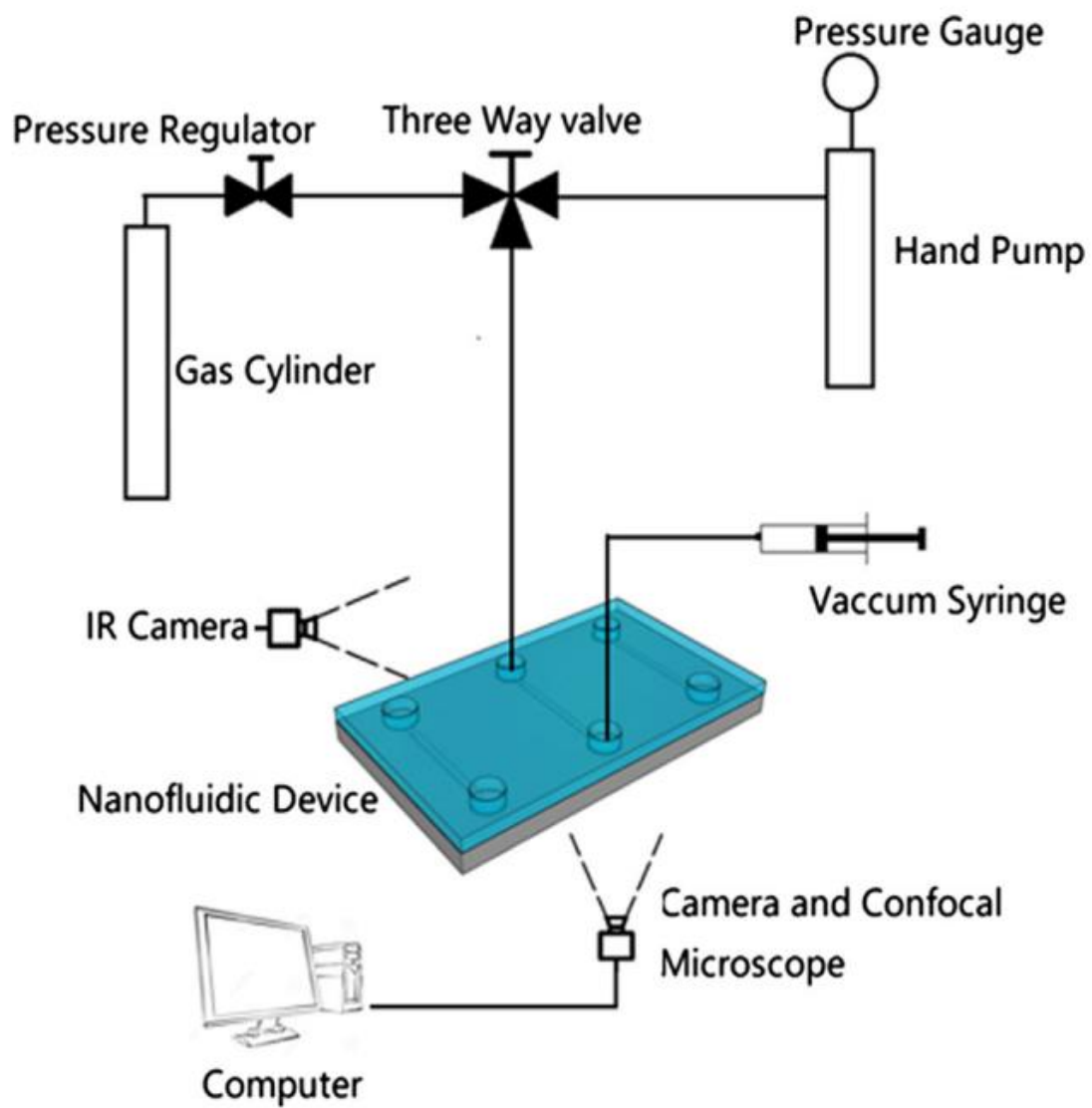
Figure 6. Schematic of the low-pressure experimental setup.
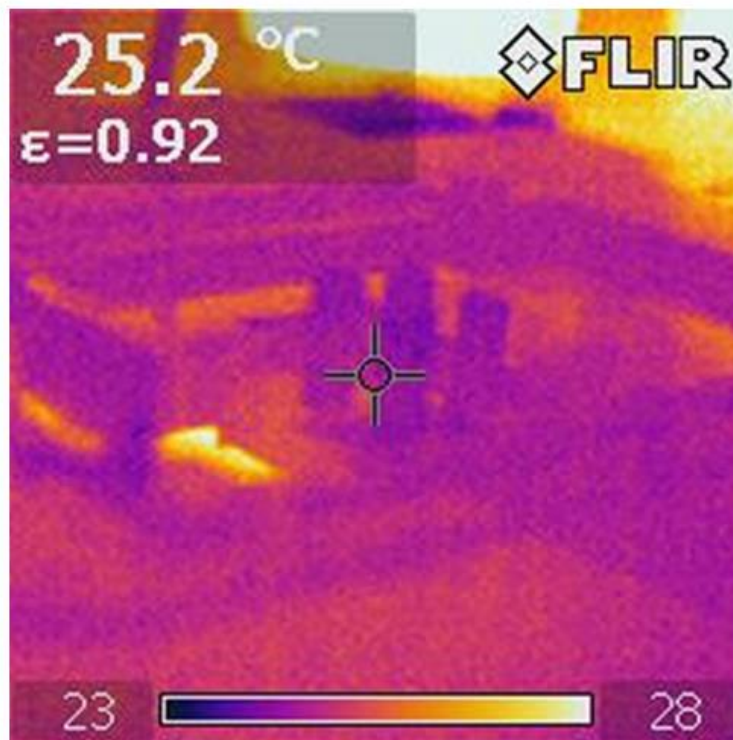
Figure 7. Temperature measurement of the nanofluidic device using IR camera.

2.2.2 High-pressure Setup

For high-pressure experiments, every piece of the equipment is selected by a specifying a minimum pressure rating of 7000 psi. ISCO 260D syringe pump from Teledyne Isco, Inc. (City, State) is used to achieve the desired pressure for performing the high-pressure experiments. This pump is rated for 7500 psi while also providing extremely small flow rates and steady injection rates, which is appropriate for the requirements of these experiments. It can also be programmed to inject at a constant flow rate or at a constant pressure. The latter is useful for holding the pressure steady during each pressure increment. The piston fluid cylinder (HIP TOC3-10, High Pressure Equipment Co., City, Sate) is used to store the piston fluid. When the piston fluid is pumped into the tubing, it acts as a piston that pushes the hydrocarbon in the tubing and suppresses the space

available for hydrocarbons and thus increasing the pressure of the system. The piston fluids in this study are either DI water or ethylene glycol, which does not physically contact or interact with the hydrocarbon. It is because of its function mechanism and its airtight nature, The piston cylinder can also be used for the controlled injection of hydrocarbon gas for potential future experiments. Following the piston fluid cylinder, the fluid stream is split into two even streams using a splitter (SS SWAGELOK UNION TEE, SS-100-3, Swagelok Company, City, State). Each of the two streams is connected to a 3-way-valve (3-WAY BALL VALVE, SS-41GXS1, Swagelok Company). For the first 3-way-valve, one side is connected to a pressure transducer (PX409-3.5KGUSBH, OMEGA Engineering, Inc.) followed by the hydrocarbon source. The other side is connected to the nanofluidic device directly. For the second 3-way-valve, one side is connected to the pressure transducer followed by the nanofluidic device and the other side is connected to the vacuum pump (RV8 115/230V, A65401903, Edwards). All experimental equipment are connected by 316 stainless steel tubing (89785K911, McMaster-Carr Supply Co.). Shut off valves (316 stainless steel ball valve, 45775K55, McMaster-Carr Supply Co.) are implemented into the system for safety purposes and better fluid flow control.

The nanofluidic device is mounted in a device manifold, and is fabricated at the Texas A&M Machine Shop. The manifold provides pressure support for the nanofluidic device for safe operation during experiments. The device is placed on the bottom plate of the manifold and is pressed down by a top plate. The copper blocks, together with block fixtures, also provide some pressure support. This prevents device failure in the vertical direction. Two copper blocks are used for temperature control. One of the copper blocks has a heating cartridge (CSH-102185/120, OMEGA Engineering, Inc.) that is inserted inside the manifold. The heating cartridge is connected

to a power supply to increase the temperature of the system during experiments. The other copper block is connected to a water-cooling system (RK012122-02, Cole-Parmer Canada Co.). The water-cooling system is used when a temperature gradient is desired. However, in this study, only the heating block is used. The assembled apparatus (consisting of the nanofluidic device mounted in the manifold) is placed under an inverted microscope (Leica DMI 6000B, Leica Microsystems Inc.) which is equipped with multiple types of optical lenses (e.g., N PLAN L 20x/0.35 and 40x/0.55 CORR objectives for imaging). A schematic of the high-pressure experimental setup is shown in Figure 8.
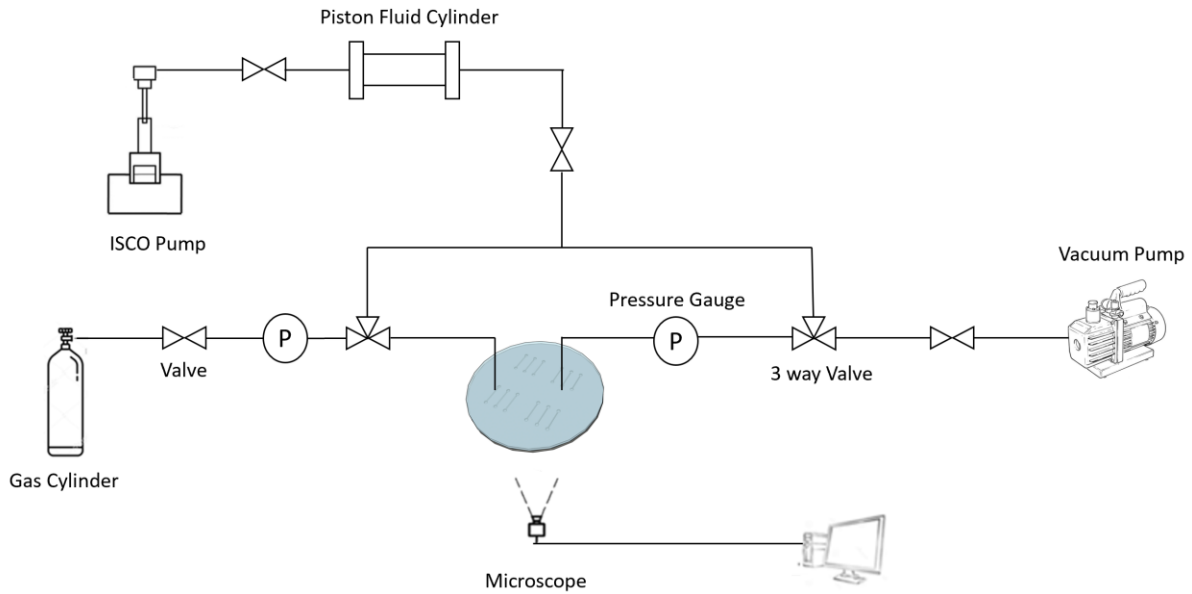
Figure 8. Schematic of the high-pressure experimental setup.

2.3 Experimental Procedure

The experimental procedure varies depending on the experimental setup. For the low-pressure experimental setup, initially, all the connectors and tubings are filled with air. This can contaminate the test fluid (hydrocarbon). Deionized water is first pumped from the water tank using a hand pump until all the tubing is filled with deionized water. The 3-way valve is then switched to connect only the n-Butane gas cylinder to the tubing that is connected to the nanofluidic device. The gas cylinder is then opened and DI water is displaced by the flowing hydrocarbon gas. This step is designed to ensure that all of the air in the tubing is eliminated. The hydrocarbon gas (n-Butane) is then allowed to flow through the tubing for 15 minutes. While the n-Butane gas is still flowing out of the tubing, the tubing is then connected to the nano-ports (that are, in turn, attached to the nanofluidic device, as shown in Figure 9. The nanofluidic device is then mounted under a confocal microscope before commencing the visualization experiments. The n-Butane gas is

28

allowed to flow through the device for 15 minutes before commencing any experiment (in order to ensure that the tubing is saturated with pure n-Butane gas). In the meantime, suction is applied using a vacuum syringe to facilitate the flow of n-Butane gas in the device.
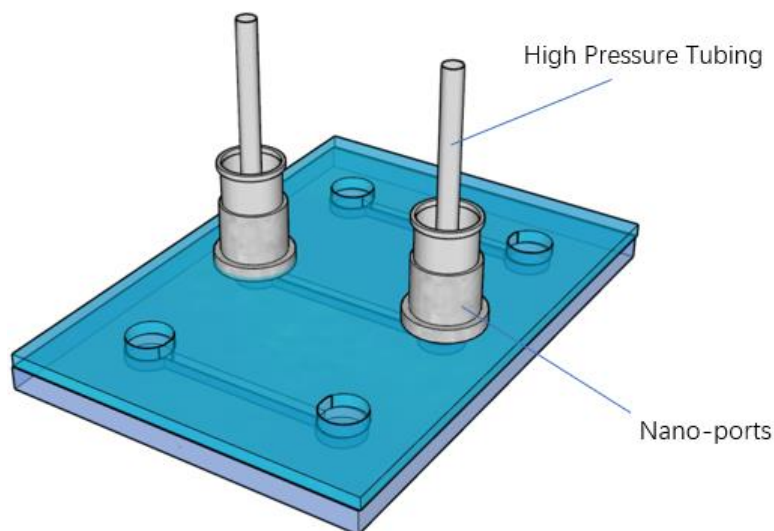
Figure 9. Schematic of nano-ports. Schematic showing the connection of the tubing to the inlet and outlet ports of the nanofluidic chips using nano-ports.

After the channels in the device are saturated with the n-Butane gas, the 3-way valve is switched back, connecting the nanofluidic device to the handpump (for pumping water). The pressure of the system is increased by pumping water into the tubing (Step d). This in turn increases the pressure of the n-Butane gas in the tubing and nanofluidic chip. The pressure is increased at a nominal rate of 0.2 psi/minute (and this is checked or recorded every minute). Once the first drop of liquid is observed under a microscope, the pressure reading from the pressure gauge is recorded as the measured value of the dew-point pressure for n-Butane. After the condensation of n-Butane is achieved completely within the nanochannel, the system pressure is slowly reduced at a rate of 0.2

psi/minute to investigate any hysteresis effects. The bubble-point pressure is recorded as the first bubble appears in the nanochannel (as observed under a microscope), while the pressure is reduced progressively (until the apparatus reverts back to atmospheric pressure). This procedure is repeated several times for multiple measurements of the dew-point pressure and bubble-point pressure values. Each measurement is repeated three times. Figure 10-12 shows the images recorded from experiments involving condensation of n-Butane in nanofluidic devices with channel depths of 10 nm, 4 nm and 2 nm respectively. In all cases, the condensation is observed to occur very fast (within a few seconds). For example, the condensation of n-Butane gas (i.e., once the dew-point pressure is reached) is observed to occur within a few seconds. For experiments involving 2 nm capillaries the condensation is observed to occur in the videos within three frames (with image acquisition rate of 1.29 second/frame).

Figure 10. Condensation process of n-Butane in 10 nm channel. Visual observation under a microscope for the condensation of n-Butane in a channel with a depth of 10 nm under room temperature conditions. (a) Channel is filled with n-Butane gas at a pressure lower than the dew-point pressure. (b) Some liquid is formed at the dew-point pressure. (c) – (e) Liquid continues to form and occupies the channel. (f) Liquid occupies the entire channel.

Figure 11. Condensation process of n-Butane in 4 nm channel. Visual observation under a microscope for the condensation of n-Butane in a channel with a depth of 4 nm under room temperature conditions. (a) Channel is filled with n-Butane gas at a pressure lower than the dew-point pressure. (b) Some liquid is formed at the dew-point pressure. (c) – (e) Liquid continues to form and occupies the channel. (f) Liquid occupies the entire channel.
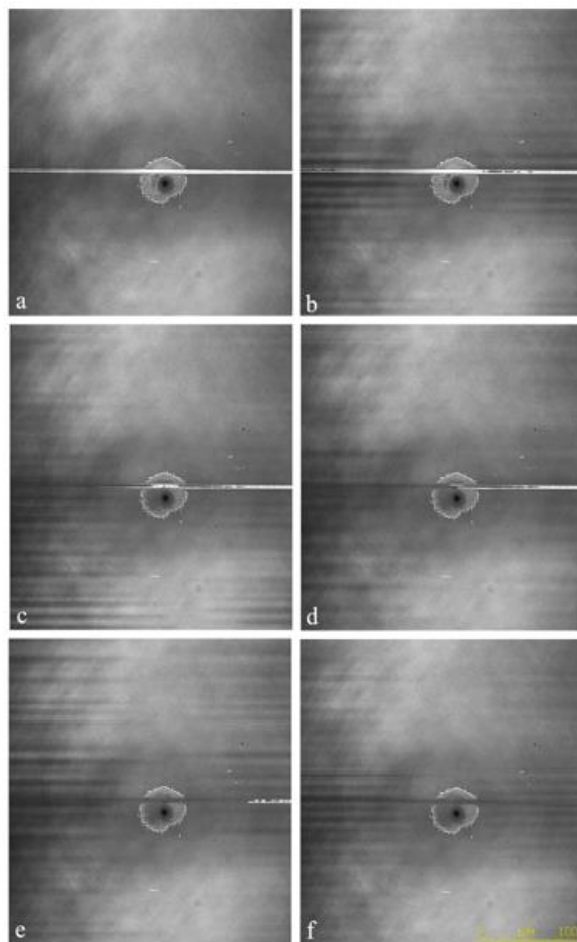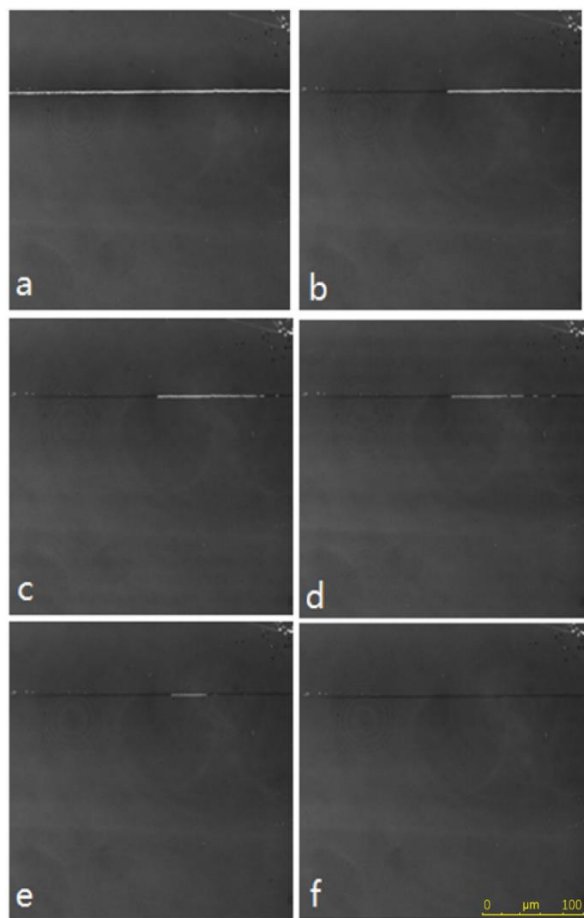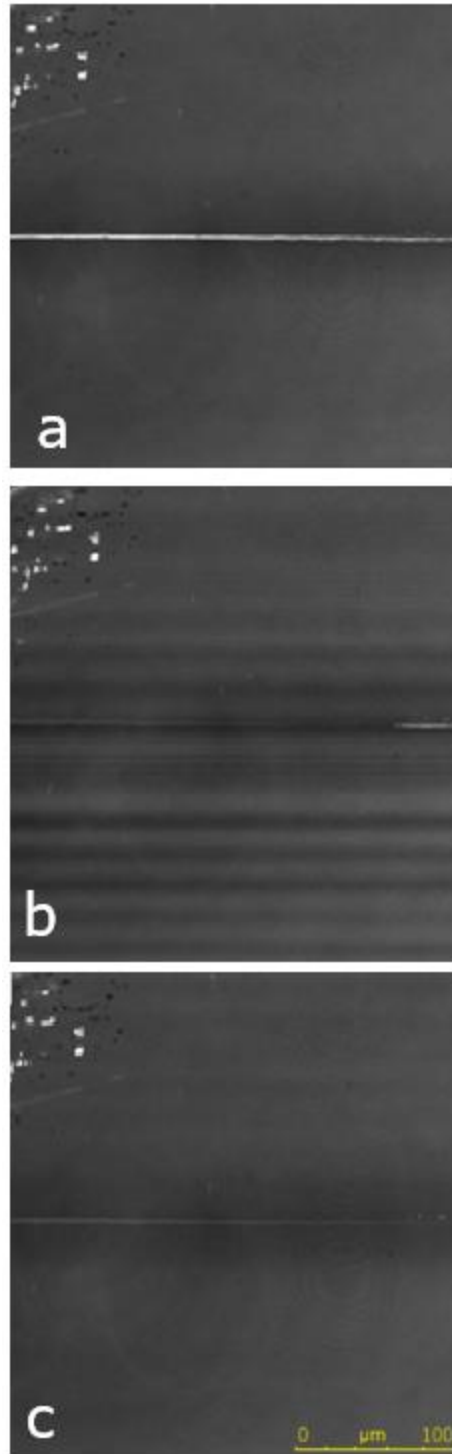
Figure 12. Condensation process of n-Butane in 2 nm channel. Visual observation under a microscope for the condensation of n-Butane in a channel with a depth of 2 nm under room temperature conditions.

For the high-pressure experiments, the workflow is shown in Figure 13. For step (a), the piston cylinder is filled with piston fluid. All the tubing from ISCO pump to the 3-way-valves are first saturated with piston fluid. The purpose of this step is to make sure that when pumping the piston fluid, flushes out all of the air trapped inside the tubing. The second step is to connect the hydrocarbon source to the nanofluidic device and the vacuum pump by adjusting the 3-way-valve openings (Step b). Then the vacuum pump is turned on. The vacuum pump is left on overnight for larger channels (i.e. channels above 4 nm in depth). The vacuum pump is sometimes left on for 24 hours or longer (depending on the readings from both transducers) for experimentsl performed using the 4 nm and 2 nm deep channels. The pressure transducers on both sides of the device are monitored and recorded during the evacuation process. A closed system is ensured and a proper vacuum setting is confirmed by monitoring the readings on the pressure transducers. If the readings of both transducers are consistent with each other and are at a pressure that is much lower than the atmospheric pressure, it implies that the system is inter-connected and there is a proper level of vacuum pressure. One more check that is implemented is to shut off the valve at the vacuum side and observe whether the pressure readings on both sides increase. If the pressure remains low and unaltered, then this approves that the system is closed and there are no leaks. Once the vacuum process is complete, the gas cylinder is opened and the hydrocarbon is allowed to flow through the device. One puff of hydrocarbon gas is enough to saturate the tubing connecting the gas cylinder and the test device. The tubing is fully saturated when the pressure transducer on the gas cylinder side has the same reading as the pressure gauge attached to the gas cylinder. As the gas flows through the experimental apparatus, the readings of the pressure transducer on the vacuum side will increase. The whole system is confirmed to be saturated with hydrocarbon gas when both pressure transducer provides the same reading. Once the gas saturation is complete, two 3-way-

valves are switched at the same time connecting the ISCO pump to the nanofluidic device (Step c). If the expected pressure measurement is below 100 psi, the pressure is quickly raised to about 10 psi below the desired pressure and the pressure is held steady for 15 minutes. For example, if the dew-point pressure for n-Butane is expected to be around 35 psi at room temperature, then the pressure will be quickly raised to 25 psi. If the expected pressure measurement is above 100 psi, the pressure will be quickly raised to about 30 psi below the dew-point pressure (in bulk environment) and is held steady for 15 minutes. The pressure is then increased at a nominal rate of 0.2 psi/minute. Once the condensation is observed under a microscope, the pressure from the pressure gauge is recorded as the dew-point pressure for n-Butane. Subsequent to the complete condensation of n-Butane within the nanochannels, the pressure is slowly decreased at a rate of 0.2 psi/minute to investigate any hysteresis effect. The bubble-point pressure is recorded as the first bubble appears in the nano-capillaries under a microscope, while the pressure is reduced progressively (until the apparatus reverts back to atmospheric pressure). This procedure is repeated several times for multiple measurements of the dew-point pressure and bubble-point pressure values. Each measurement is repeated three times.

For the measurement of the dew-point pressure of hydrocarbon at different temperatures, each experiment commences at room temperature. Once a set of measurements are acquired, the temperature of the apparatus is increased by either the adhesive heater (Kapton Insulated flexible heater, KHLV-0502, OMEGA Engineering, CO.) that is attached directly onto the nanofluidic device or using the heating block that is inserted in the apparatus along with the heating cartridge. The power input is maintained at a constant value for each step and the temperature is monitored by the IR camera to confirm that steady temperature conditions are achieved during the

experiments. Figure 14 shows the images recorded from experiments involving condensation of

n-Butane in nanochannels that were performed using the high-pressure experimental setup.
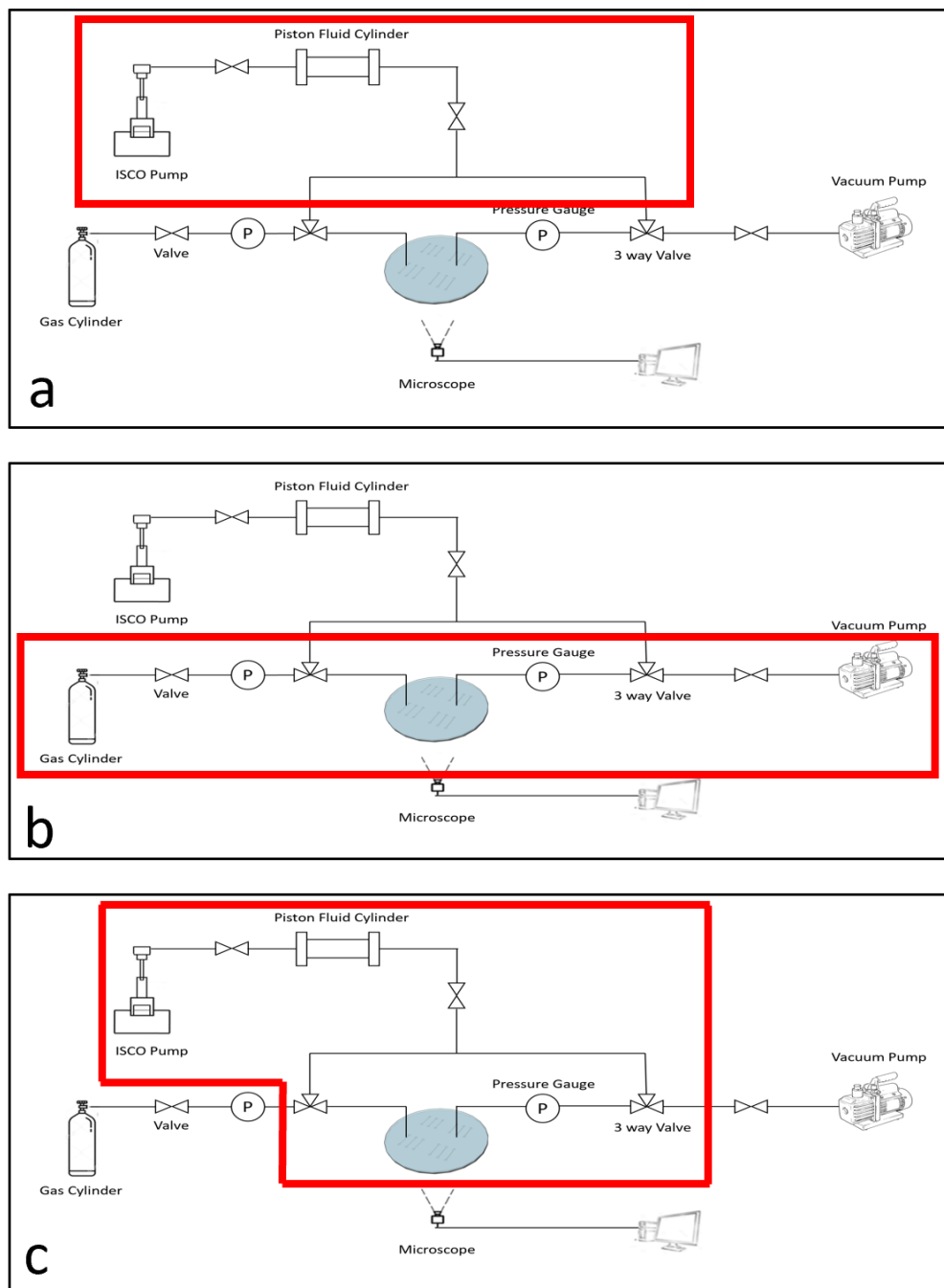
Figure 13. Experimental procedure for high-pressure experiment.
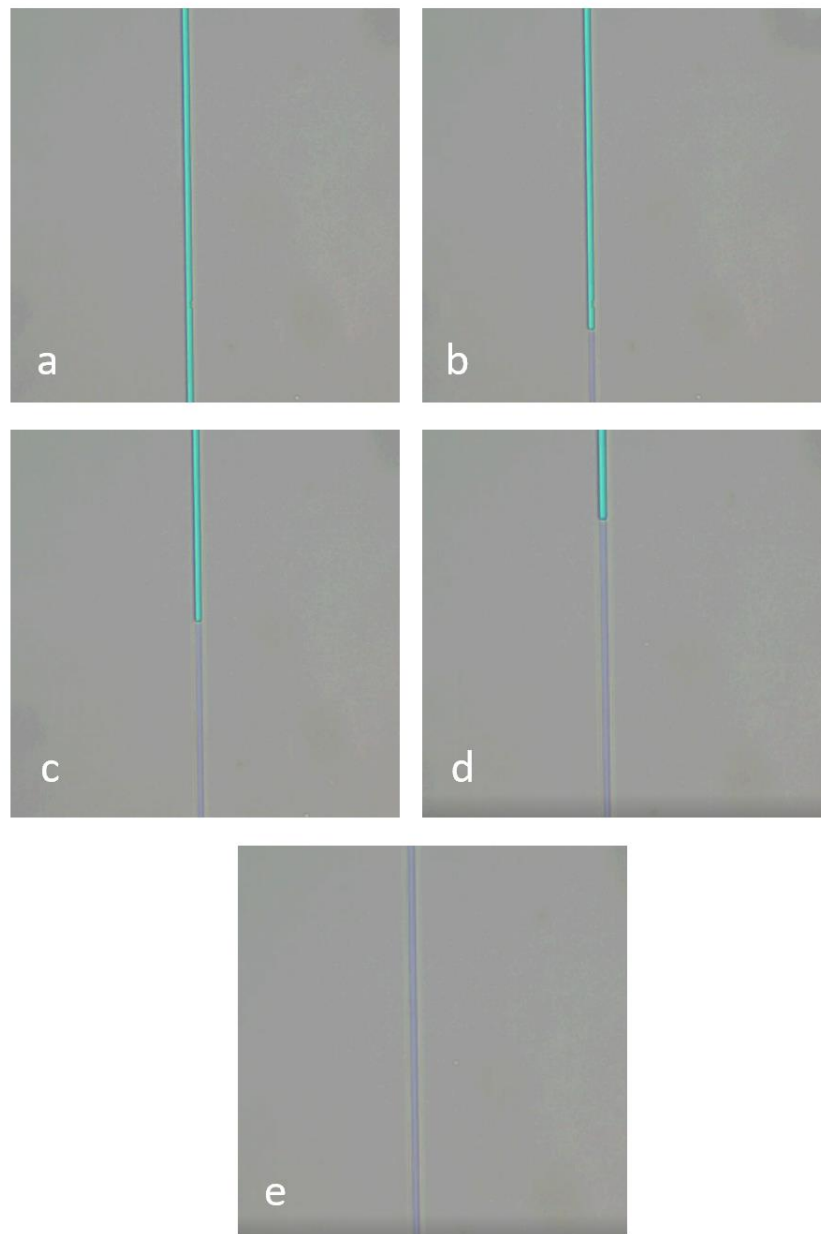
Figure 14. Condensation process of n-Butane in 10 nm channel with elevated temperature.
Visual observation under a microscope for the condensation of n-Butane in a channel with a depth of 10 nm. (a) The channel is filled with n-Butane gas (light blue) at a pressure lower than the dew-point pressure. (b) – (d) Liquid (dark blue) continues to form and occupies the channel. (e) Liquid occupies the entire channel.

The piston fluid has the same color as liquid n-Butane and it is difficult to distinguish between them, especially when the condensation is continuous (i.e. the condensation happens from one end of the channel to the other end of the channel). However, the presence of the test fluid inside the channel can be distinguished by its phase-behavior once the temperature is increased. In the experiment where the temperature of the system is elevated after condensation at a lower temperature, it is observed that the fluid is vaporized into the gas phase everywhere inside the channel shortly after the temperature is increased. The pressure readings when the temperature is elevated are at 32.08 psi and 125.94 psi. The vaporization temperature for the piston fluid, which is water, is 257.5 °F and 344.94 °F respectively. The required temperature for phase-change of water is much higher than the elevated temperature imposed in the experiments and therefore, the fluid that is vaporized can be distinguished (or confirmed) as n-Butane.

3. RESULTS AND DISCUSSION[*]

3.1 Nanofluidic Device Characterization

Nanofluidic device characterization is a crucial step during the fabrication process to ensure the proper implementation of the designed features. This section showcases the results for the profile of the nanofluidic devices that are used in the experiments.

The nanofluidic devices fabricated in Aggiefab are characterized using two different equipment. The first one, Bruker DektakXT Surface profiler, can be used in the measurements of deeper channels or as a preliminary measurement for smaller features. Figure 15 showcases the channel profiles of some of the deeper channels fabricated on a silicon wafer.

---

[*] Part of the data reported in this chapter is reprinted with permission from "Direct visualization and molecular simulation of dewpoint pressure of a confined fluid in sub-10 nm slit pores" by Yang, Q., Jin, B., Banerjee, D., & Nasrabadi, H., 2019. *Fuel, 235*, 1216-1223. Copyright [2018] by Elsevier Ltd.
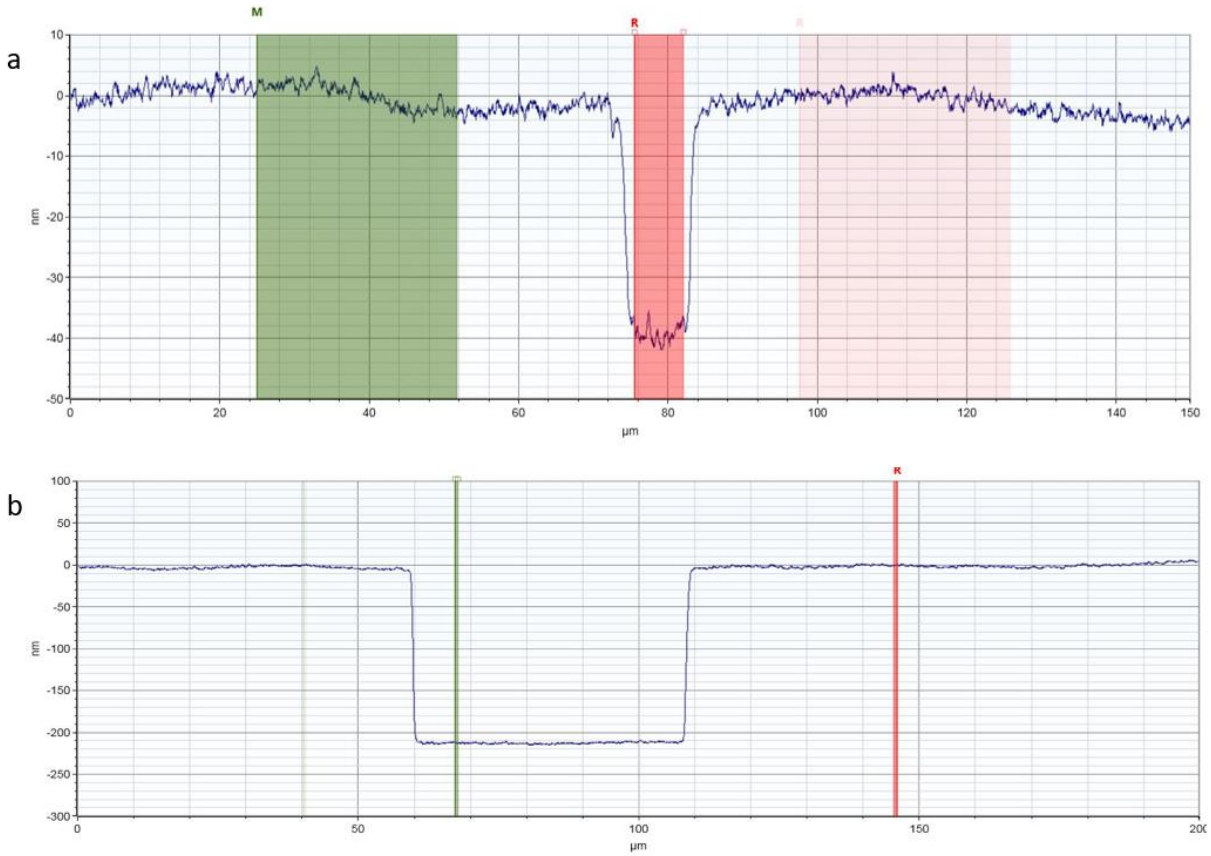
Figure 15. Profile of the channel and reservoir by Bruker DektakXT Surface profiler. (a) profile of the 40 nm channel. (b) profile of a reservoir that is connected to the channel

A more precise surface scan that is required for shallow features, for example, channels smaller than 10 nm, can be performed by using another equipment Bruker Dimension Icon Atomic Force Microscope. Figure 16-22 are the profile measurement of fabricated nanofluidic devices.
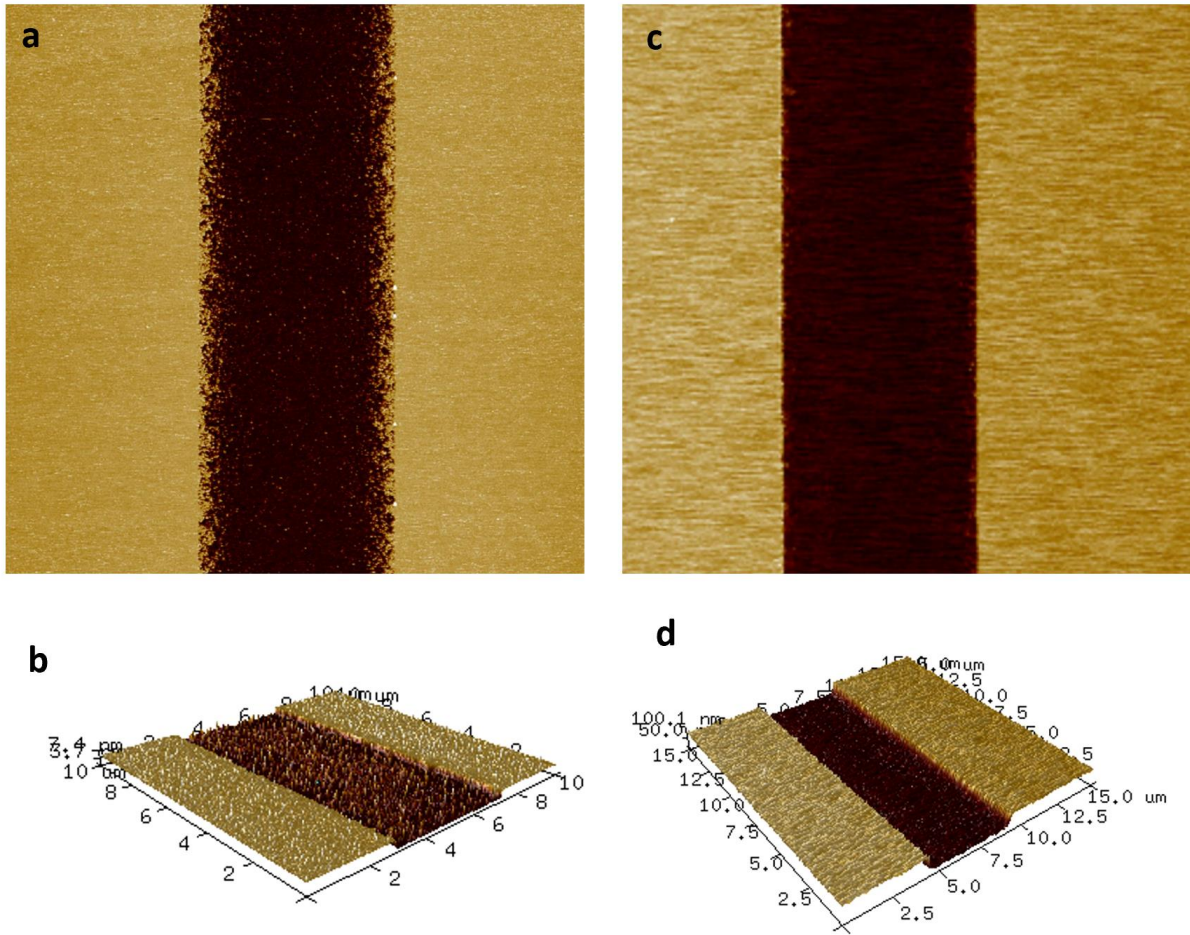
Figure 16. Surface profile of the etched channel by Icon AFM. (a) surface scan of a 10 nm channel. (b) 3D image of the 10 nm channel. (c) surface scan of a 50 nm channel. (d) 3D image of a 50 nm channel.
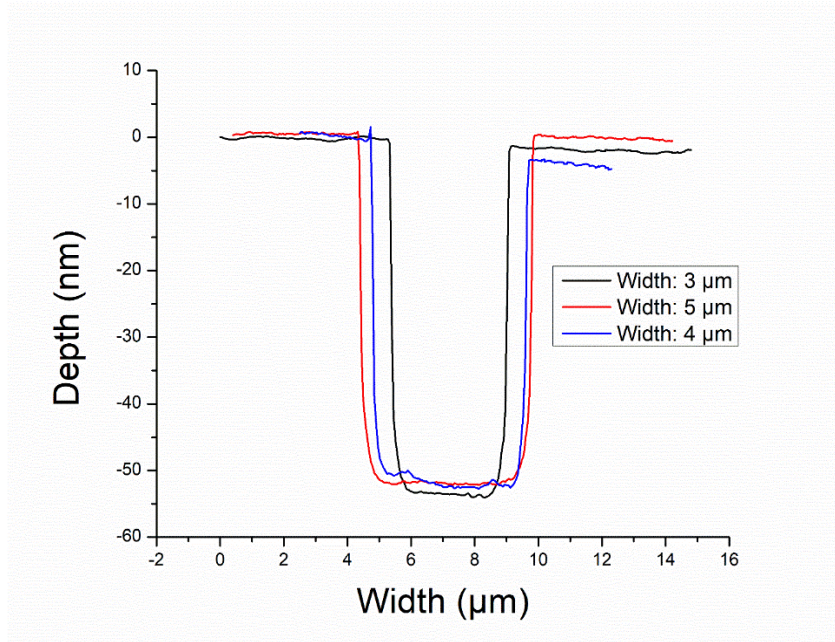
Figure 17. Depth profile of 50 nm channels.
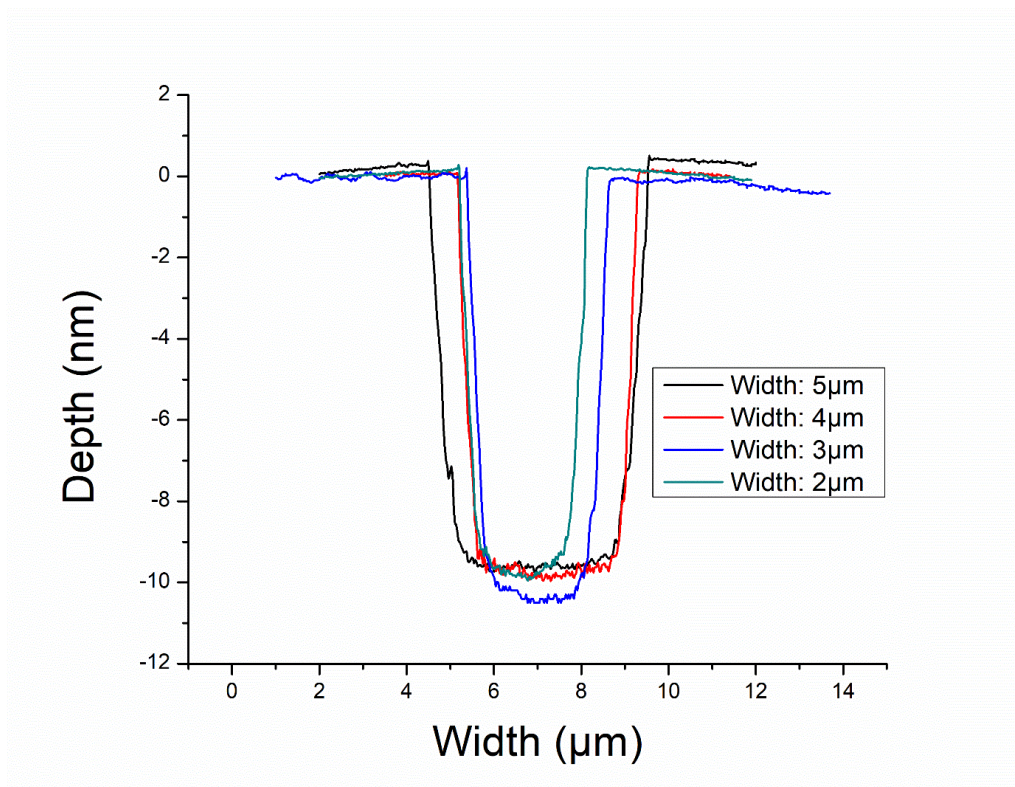
Figure 18. Depth profile of 10 nm channels.
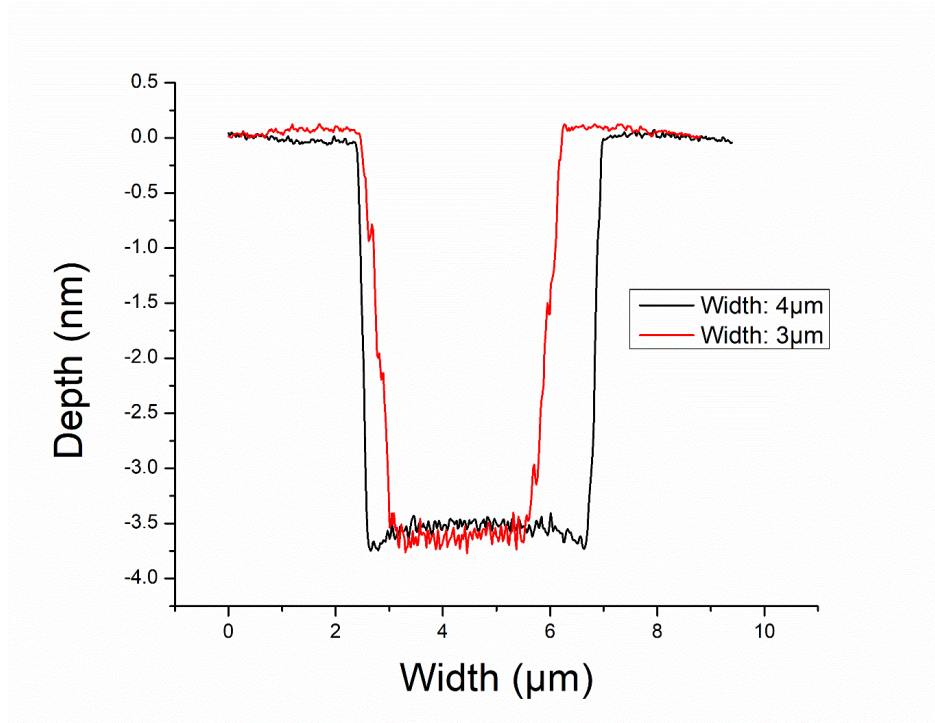
Figure 19. Depth profile of 3.5 nm channels.
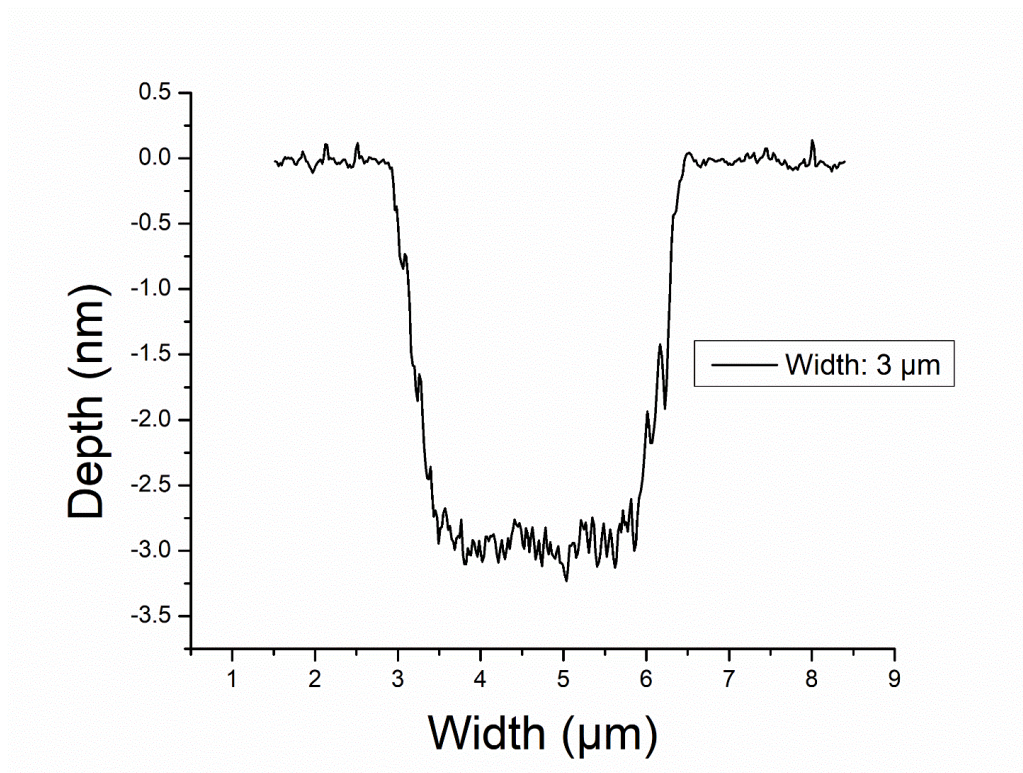
Figure 20. Depth profile of 3 nm channels.
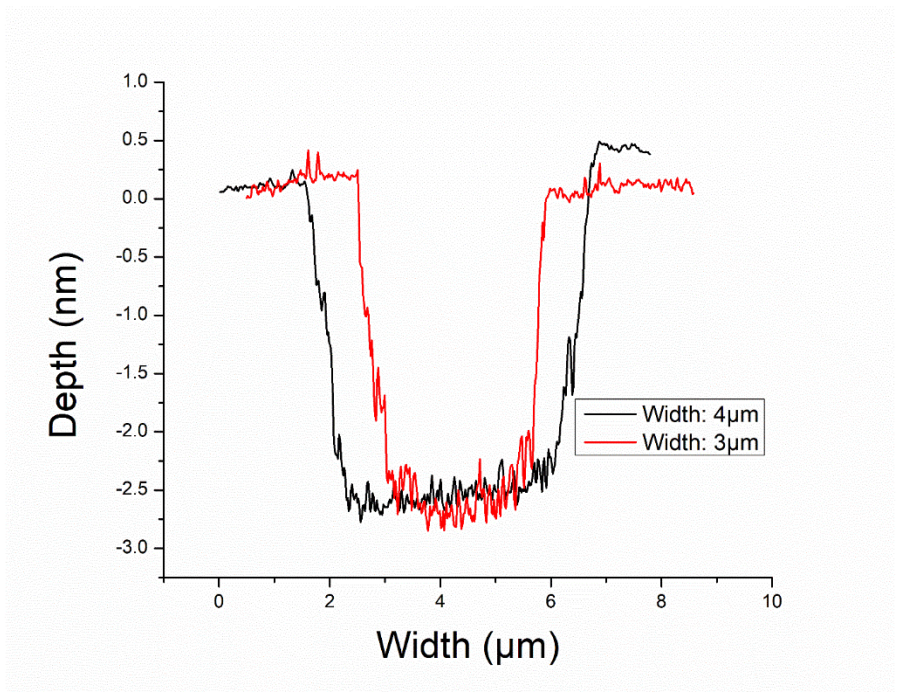
Figure 21. Depth profile of 2.5 nm channels.
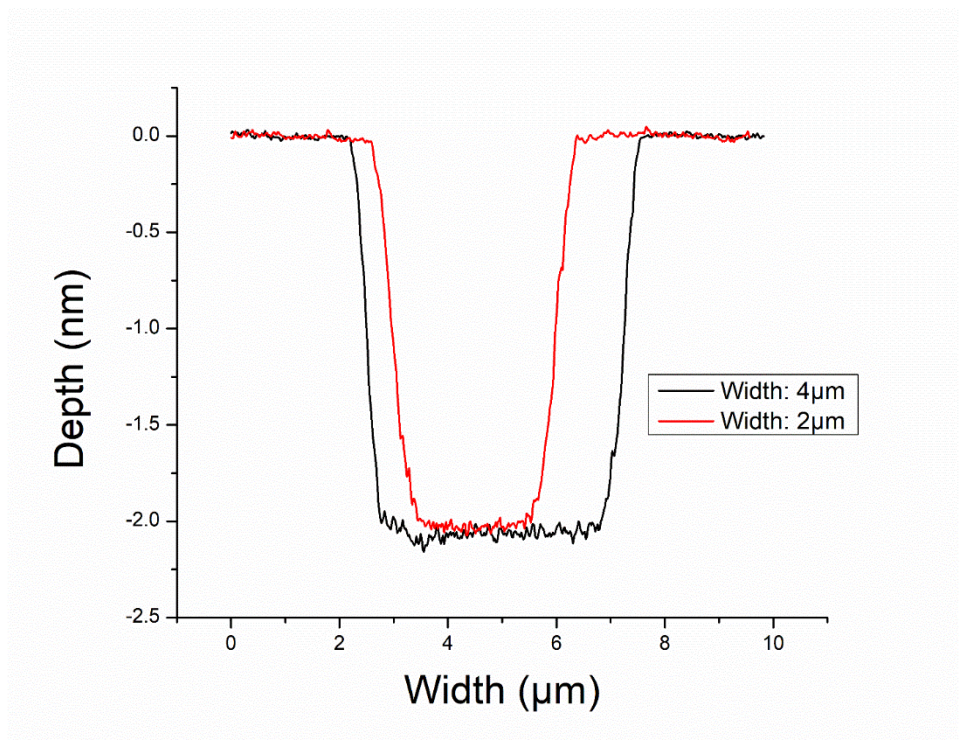
Figure 22. Depth profile of 2 nm channels.

The fabrication steps are not always successful. Sometimes the yield from a particular process step can be deficient. The overall yield was calculated from all the fabricated devices and is estimated to be around 30%. There are three major ways a device can fail. The most common is that a channel can have edges protruding out, as shown in figure 23. The protruding edge may not cause a problem during the bonding process if the feature size is large. However, when the channels are small (for example, shallow and narrow channels), the protruding part on edge can be crushed down into the channel and block the channel during the bonding process. This protruding edge phenomenon is speculated to be caused by the remaining photoresist that is stuck along the edge. The photoresist can be extremely hard to remove in the experiment after hard baking and reactive ion etching process. Piranha solution cleaning has been applied trying to remove the protrusion but the outcome is not very effective. Another possibility is that the protrusion can be caused by the etching process which cannot be controlled. Another deficiency is the rough surface on the wafer surface as shown in figure 24. A rough surface can have hills and valleys that are 10 nm in height and makes the sub-10 nm features meaningless. This is found out to be caused by the plasma enhanced chemical vapor deposition process where a silicon dioxide layer is deposited onto the silica wafer. This problem can be solved by another way of generating a silicon dioxide layer, which is wet oxidation. Wet oxidation is preferred for generating a thin film of oxide on the silicon wafer surface since it helps to minimize the surface roughness to less than 0.5 nm.

Another deficiency is missing features or wider channels than expected, as shown in Figure 25. Sometimes the design has four columns of pillars in the middle but, at the time of process completion, only two survived. Other times the channels are designed to have a width of 3 µm, but at the time of process completion, the channel is measured to be 5 µm wide. This may cause a

problem (channel collapsing) if the process conditions are sensitive to the channel width. These two phenomena are believed to be caused by the variations in the photolithography and etching process conditions. If the photoresist is over exposed during the photolithography process, some of the photoresist that is not supposed to be removed will be removed, exposing more of the silicon dioxide underneath and causing more features to be etched away. The over exposure of photoresist can be caused by many reasons. For example, the dose of the exposure may be too high, or the thickness of the photoresist is incorrect prior to soft bake, or the quality of the soft bake is not sufficient. However, these procedures and parameters can be controlled and optimized to reduce the chance of deficiency during fabrication.
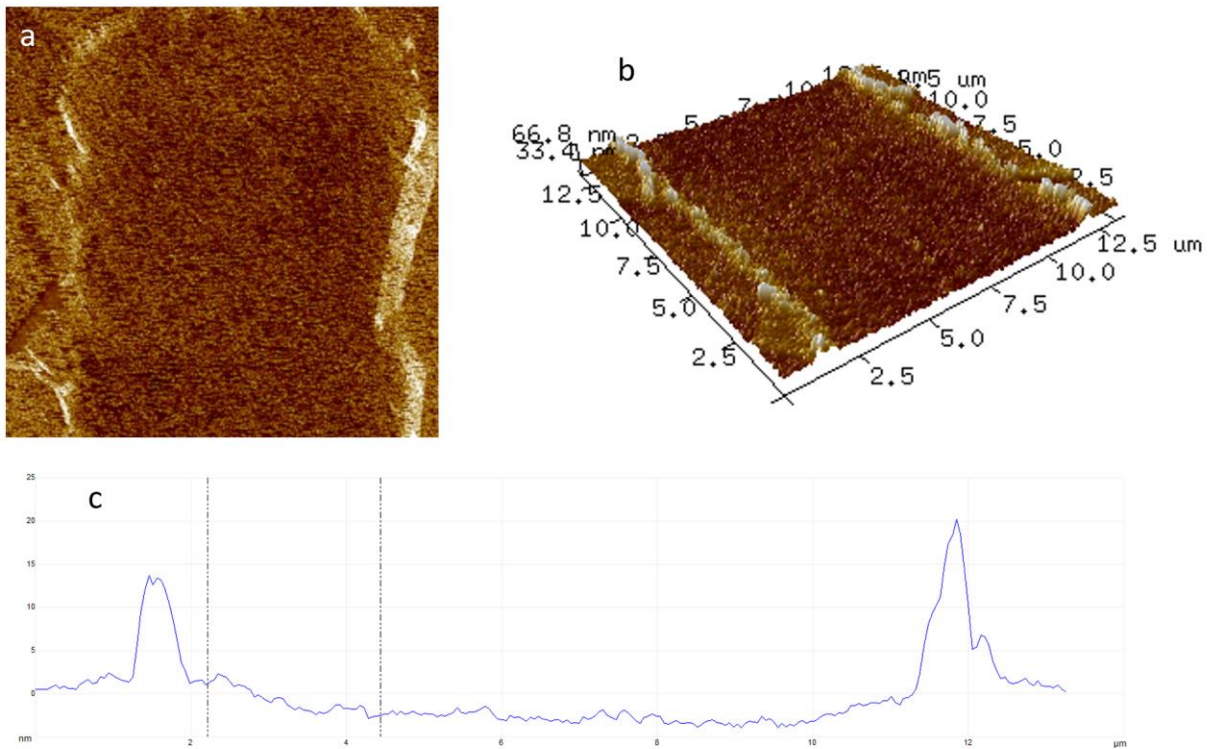
Figure 23. Etched channel with a protruding edge by AFM. Image acquired using AFM for the dimensions of the etched channel showing that protrusions formed on the edges. (a) the surface

scan of the channel. (b) the 3D image of the scanned surface. (c) cross-section profile of the etched channel.
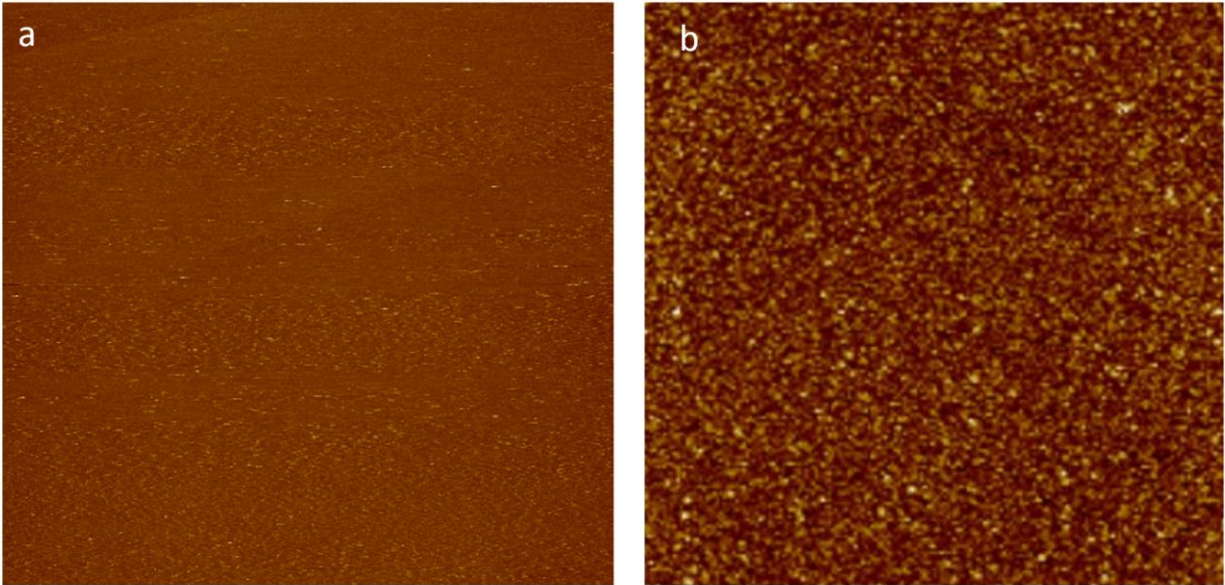
Figure 24. Surface roughness scan of the etched wafer from AFM. (a) the surface of the wafer with wet oxidation. The surface roughness is extremely small and the surface is very smooth. (b) the surface of the wafer after PECVD. The surface is very rough with peaks and valleys of 10 nm height.
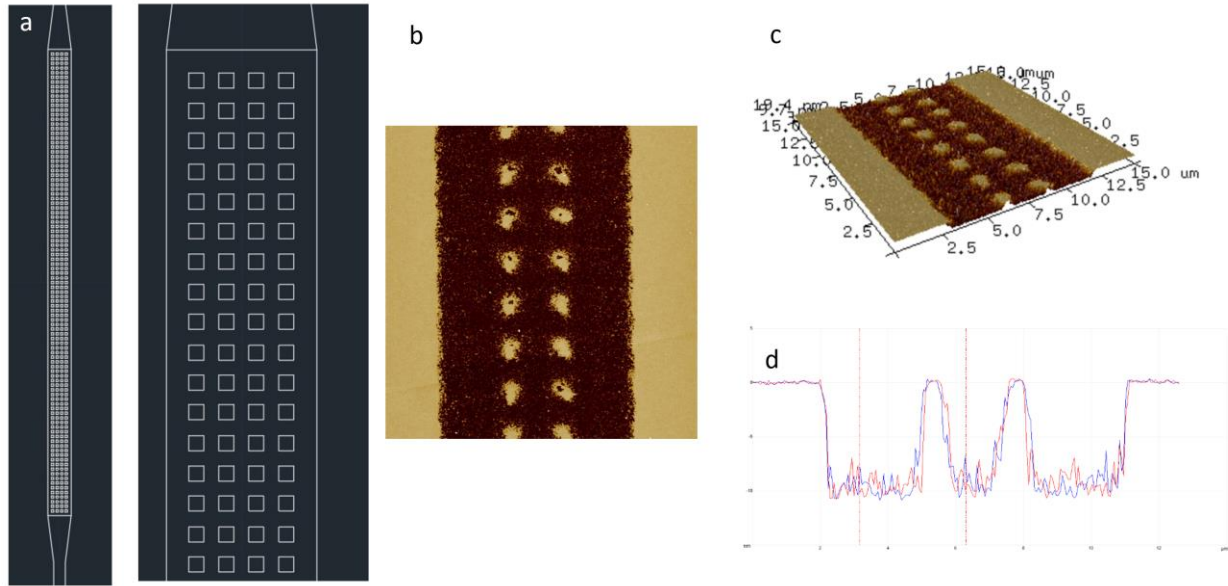
Figure 25. Surface scan of a more complex pattern by AFM. (a) the original design of the pattern with 4 columns of pillars in the middle. (b) the surface scan of the channel showing only 2 columns of pillars. (c) the 3D image of the scanned channel. (d) the depth profile of the scanned channel.

3.2 Device Pressure Tolerance Test

Two types of glass wafers are used during the fabrication steps: 0.5 mm thick and 2 mm thick. Pressure tolerances of both devices have been tested by pumping water into the device with ISCO pump until device breakdown (or cracks) are observed. Figure 26 shows the pressure recordings of the pressure test. From the data it can be concluded that the 2.0 mm thick glass wafer can tolerate about 1000 psi and the 0.5 mm can tolerate about 70 psi. A cracked device with the thicker glass wafer is shown in Figure 27. In the picture the device is broken into four pieces where the crack is observed to be initiated from a single point. For all four pieces, the bonding between the glass layer and the silica wafer did not break. This demonstrated that the bonding strength is sufficient

48

but the weakest point of the device is located in the glass wafer and the strength of the glass wafer is the limiting parameter. There are two major ways that can improve the strength of the device. The first one is by further increasing the thickness of the glass wafer. But as mentioned before in the fabrication section, a thicker glass wafer would require higher values of voltage and temperature to be imposed during the wafer bonding process, which in turn would limit the feature sizes that can be fabricated within the device. Also, a thicker glass wafer can also limit the optical access under the microscope lenses when the experiments are performed under a microscope as high-resolution lenses usually have a shorter working distance (distance from a lens to the focused object). If the glass layers are too thick, high-resolution lenses will be impossible to use. For example, a 40X lens apparatus has a working distance of about 2.5 mm and therefore, will not be suitable for glass wafers thicker than about 2 mm. Another way to achieve a higher operating pressure without increasing the thickness of the glass layer is by designing and optimizing the dimensions of the manifold for mounting the devices during the experiments. The manifold currently used in this study is rectangular shaped and can be optimized for circular shaped wafers. A new manifold with a chamber that matches the size of the device exactly can be designed, machined and utilized during the experiments. With better manifold support, the device can be expected to operate at much higher pressures.
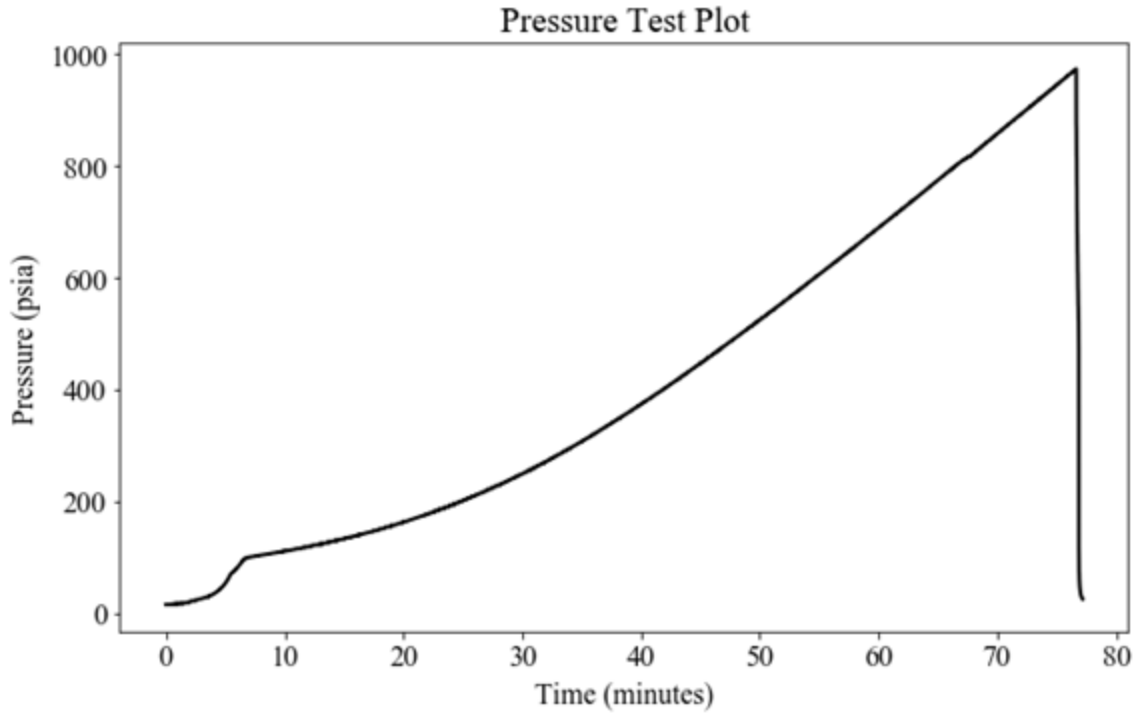
Figure 26. Pressure testing record of the device with 2 mm thick glass. The device failed at about 970 psi.
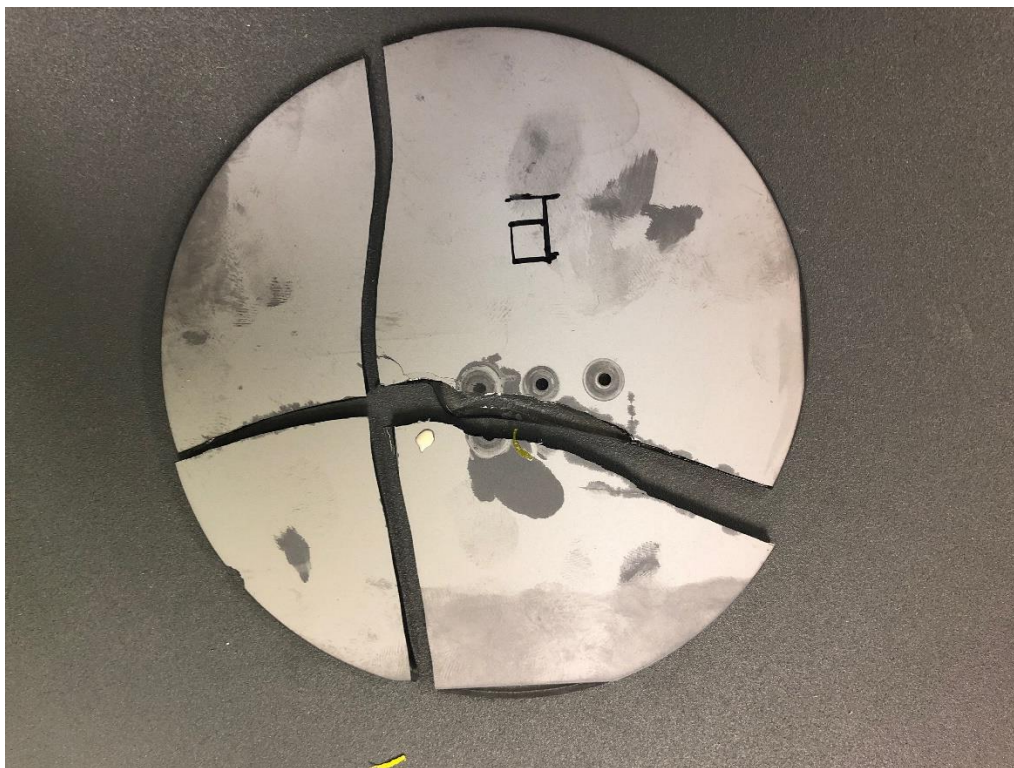
Figure 27. Picture of the failed device.

3.3 Dew-point Pressure Measurements in Nano-Channels

3.3.1 Measured Experimental data

The results for dew-point pressure of n-Butane for all nano-channels under room temperature conditions are shown in Figure 28. The measurements and the experimental uncertainties are listed in Table 2. A set of high-pressure experiments were conducted with n-Butane in 10 nm channels with elevated temperature. Three different temperatures are chosen ranging from room temperature to typical reservoir temperature and their respective dew-point pressure measurements with experimental uncertainty are shown in Figure 29 and listed in Table 3. The calculation of the experimental uncertainty is demonstrated in the following section. The n-Butane dew-point

51

pressure at 25.2 °C is at 35.5 psia under bulk conditions, according to the National Institute of

Standards and Technology (NIST)[107] . The measured dew-point pressure for the 50 nm channel

is very close to the dew-point pressure value (for bulk quantities of fluid), which validates the

experimental method adopted in the study (this is expected as the confinement effect starts to

dominate for capillary sizes less than 10 nm). As the capillary size is decreased from 50 nm to 2

nm the confinement effect is more pronounced (i.e., the dew-point pressure starts to deviate

significantly from the bulk properties reported in the literature, as shown in Figure 28).
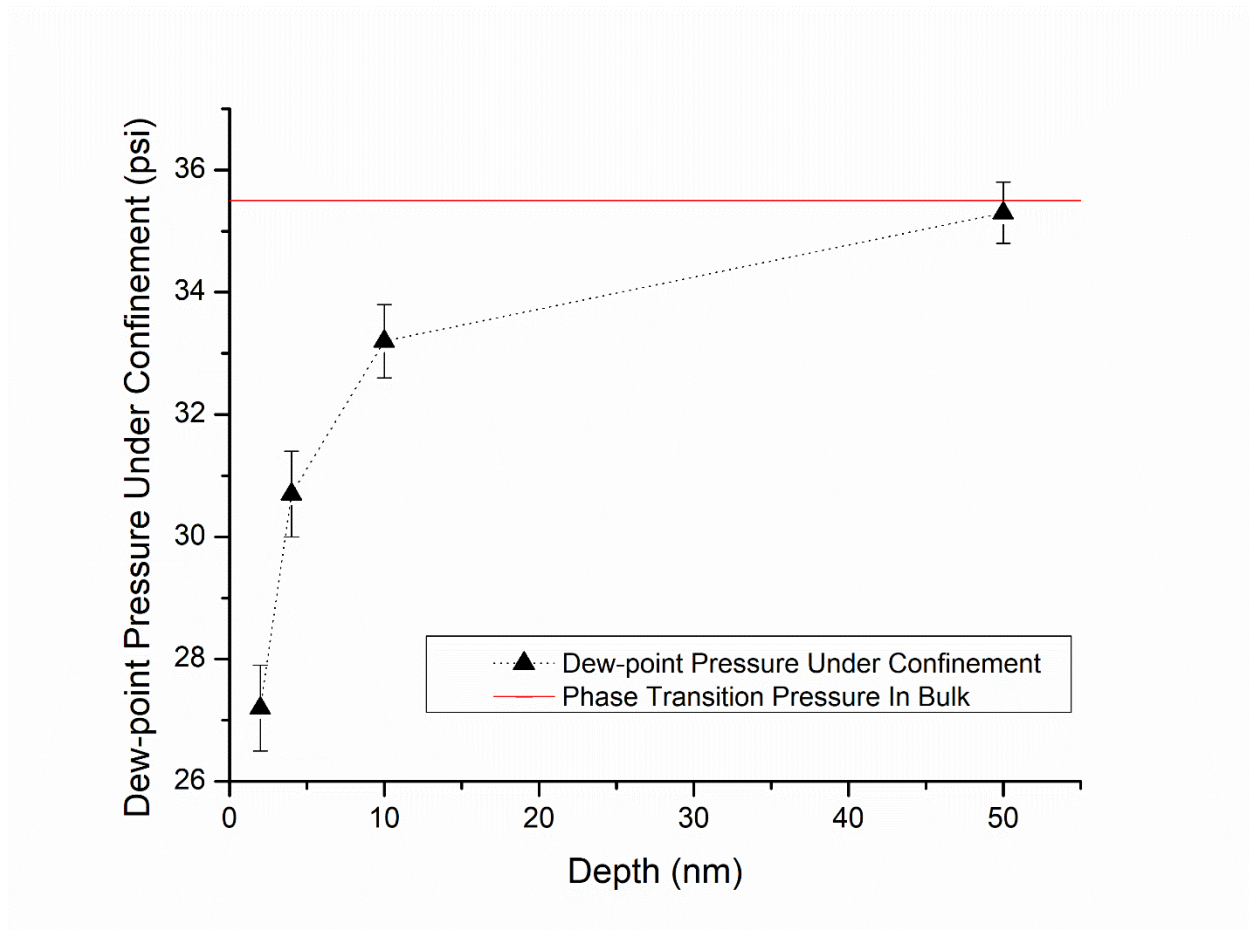
Figure 28. Experimental dew-point pressure measurement data under confinement effect.

Table 2. Room Temperature dew-point pressure measurements. Experimental uncertainty is

listed in brackets

Depth, nm	Dew-point Pressure, psia
50	35.3 (0.9)
10	33.2 (0.9)
4	30.7 (0.7)
2	27.2 (0.8)
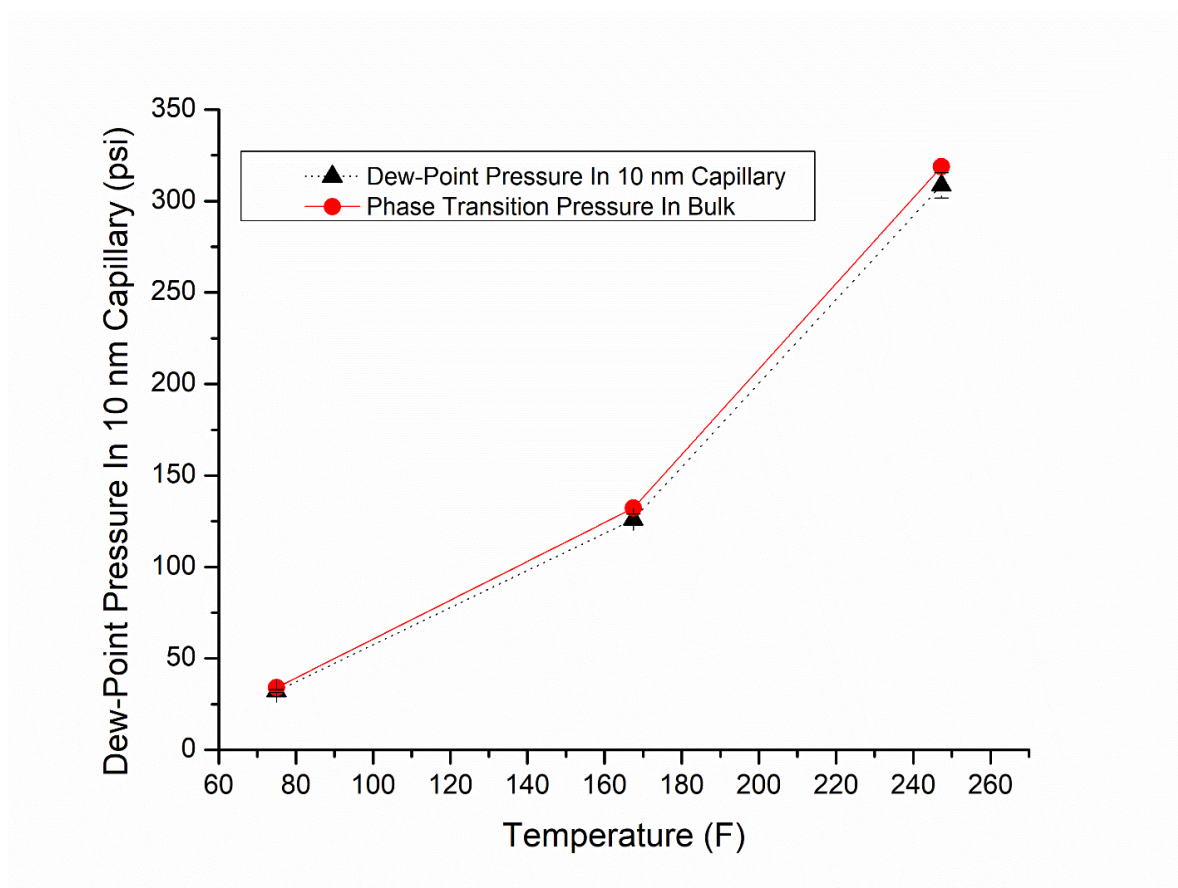
Figure 29. Experimental dew-point pressure measurement data with elevated temperature.

Table 3. Dew-point pressure measurements under elevated temperature environment.

Experimental uncertainty is listed in brackets

Temperature, °F	Dew-point Pressure, psia
75	32.08 (0.76)
167.5	125.94 (2.98)
247.3	308.55 (6.92)

The percentage of deviation for the values of the dew point pressure obtained from NIST database with that of the experimental data are shown in Table 4 and Table 5. The results listed in Table 4 show that the deviation between NIST data and experimental data (obtained in this study) is negligible for channel depths of 50 nm (thus showing that deviation due to confinement effect is negligible in this case). However, Table 4 shows that the confinement effect is highly pronounced for the channel depth values of 4 nm and 2 nm (where the deviation is 13.5% to 23.4%, respectively). For the data with elevated temperature experiment set, the measured percentage deviation at low temperature is very close to the room temperature experimental data. However, as the temperature increases from room temperature to the reservoir temperature, the confinement effect becomes less pronounced.

Table 4. Deviation in the values of Dew-point pressure for low pressure experiment. Comparison between data obtained from NIST Database with that of the Experimental Data (Figure 28)

Depth, nm	Measured Dew-point Pressure, psi	Dew-point Pressure Deviation, %
50	35.3	0.6
10	33.2	6.5
4	30.7	13.5
2	27.2	23.4

Table 5. Deviation in the values of Dew-point pressure for high pressure experiment. Comparison between data obtained from NIST Database with that of the Experimental Data (Figure 29)

Temperature, °F	Measured Dew-point Pressure, psi	Dew-point Pressure from NIST, psi	Dew-point Pressure Deviation, %
75	32.08	34.08	5.9
167.5	125.94	132.24	4.8
247.3	308.55	318.77	3.2

3.3.2 Measured Experimental data Compared with Kelvin Pressure

The phase transition pressure is also calculated and compared with the experimental data using Kelvin Equation:

$$P_{eq} - P_s - \frac{RT}{V_m} \ln \frac{P_{eq}}{P_s} = \frac{\gamma}{r} \qquad (3)$$

In the equation above, P_s is the standard saturation pressure at temperature $T = 25.2$ °C, P_{eq} is the equilibrium pressure for capillary condensation with a curved meniscus, R is the universal gas constant, V_m is the molar volume of the liquid [107], γ is the interfacial tension, and r is the radius of curvature of the liquid-vapor interface which is calculated with equation:

$$\frac{1}{r} = 2(\frac{1}{w} + \frac{1}{d}) \qquad (4)$$

Here w is the width of the channel and d is the depth of the channel. Parameters used in Kelvin Equation are obtained from NIST are listed as follows. The results are shown in Figure 30.

$$P_s = 35.5 \ psia$$

$$V_m = 0.10152 \ l/mol$$

$$\gamma = 0.01179 \ N/m$$
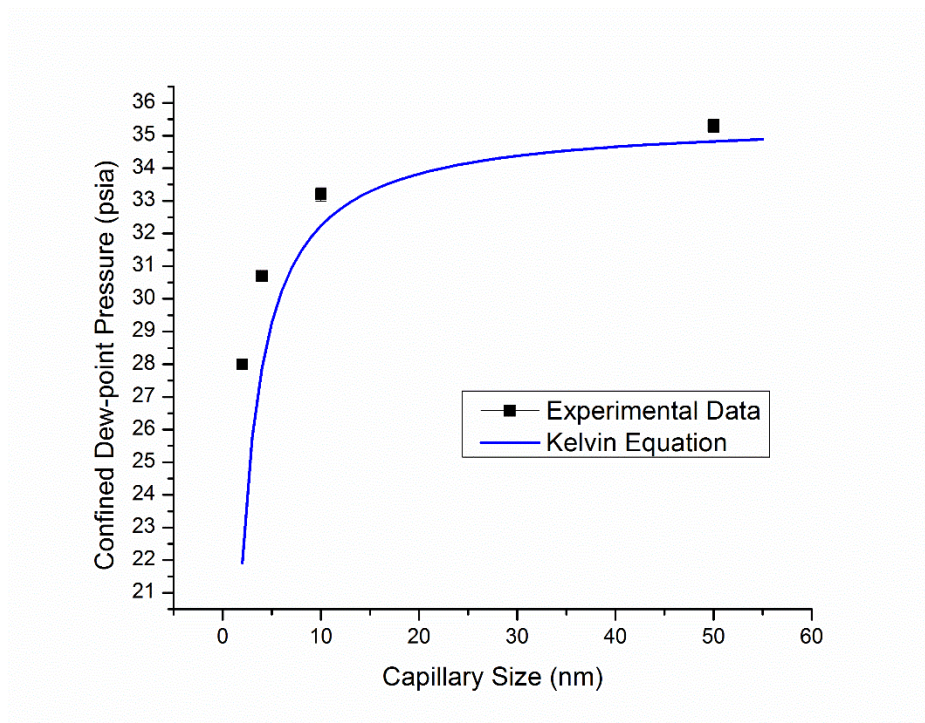
Figure 30. Comparison between low pressure experimental results and Kelvin Equation.

For phase transition pressure calculated from Kelvin Equation for the elevated temperature experiment, the temperature dependent parameters used are listed below in Table 6 obtained from NIST. The results are shown in Figure 31.
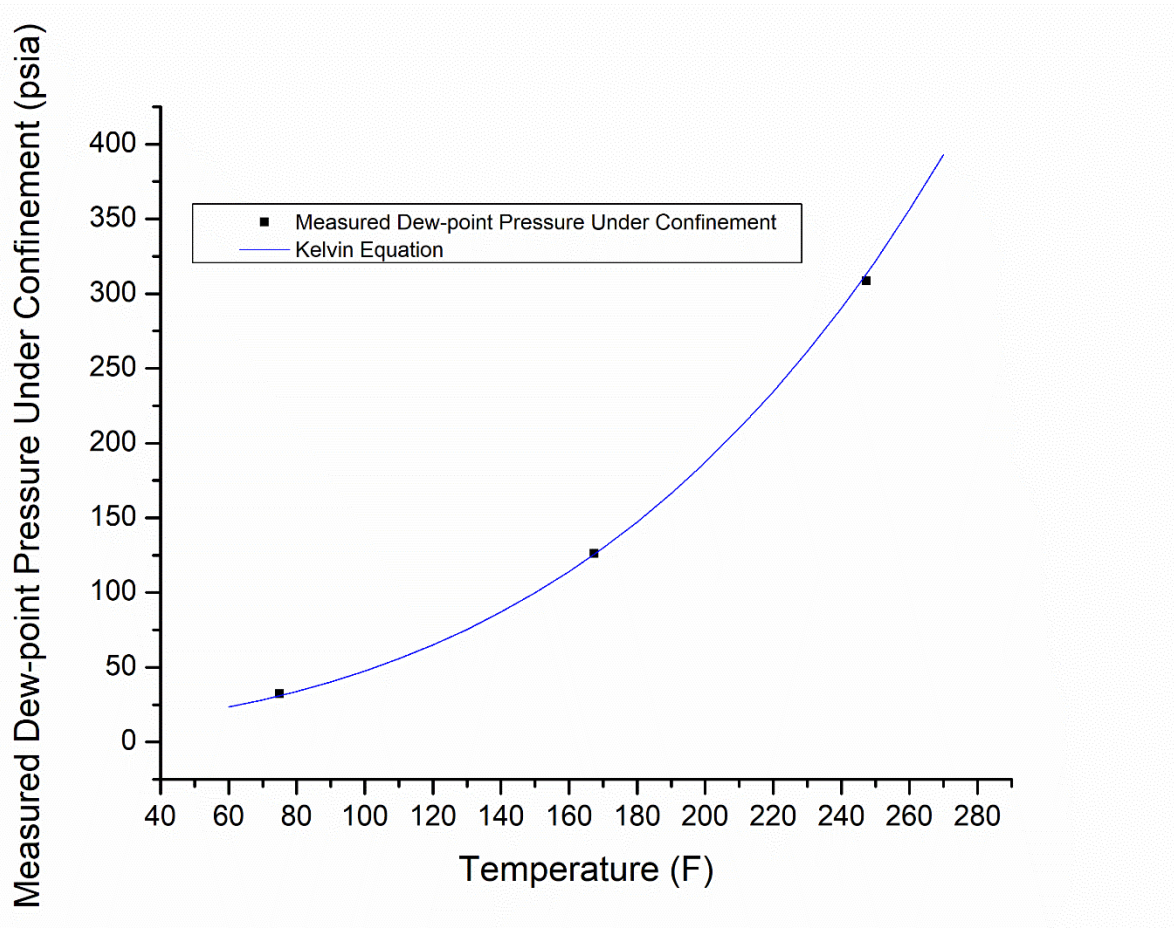
Figure 31. Comparison between high pressure experimental results and Kelvin Equation.

The accuracy of the Kelvin Equation (Eq. 3) is evaluated for different values of channel depth. For room temperature experiment, the deviation of the experimental data for the values of dew point pressure (compared to that of the predictions from the Kelvin Equation, (Eq. 3) for n-Butane for various values of channel depth are shown in Table 7 (Fig. 34) The percentage values for the deviation are indicative of the acuteness of the confinement effect. The results show that when the channel depth is above 10 nm the confinement effect (i.e., the percentage deviation for the value of dew point pressure between model prediction and experimental data) is not significant. However, as the channel depth is decreased below 10 nm (i.e., when the channel depth is in the

same order of magnitude as the size of the n-Butane molecules), the confinement effect is more pronounced (i.e., as the channel depth is reduced below 10 nm the percentage deviation for the value of dew point pressure between model prediction and experimental data increases significantly, with the deviation ranging from 9% to 22%; as the channel depth is reduced from 10 nm to 2 nm).

As for the high-pressure experiment, Kelvin Equation gives a better matching as the temperature of the system increases as shown by Table 8 (figure 31). At lower temperature, the predicted kelvin equation underestimates the phase transition pressure by a few percentiles. But as temperature increases, the predicted Kelvin Pressure becomes closer and closer to the experimental data. At a temperature of around 167.5 ˚F, the two values are extremely close to each other (second data point). When the temperature is raised further, Kelvin Equation prediction tends to overestimate the condensation pressure by a few percentiles.

Table 6. Parameters used in Kelvin Equation calculation for different temperatures.

Temperature, F	Interfacial Tension, N/m	Molar Volume, l/mol
75	0.011982	0.10129
167.5	0.0062622	0.11452
247.3	0.0021252	0.13626

Table 7. Deviation of dew-point pressure of the Kelvin Equation. Deviation in the values of Dew-point pressure for predictions of the Kelvin Equation (Eq. 3) with that of the Experimental Data (Figure 30)

Depth, nm	Kelvin Equation Pressure, psia	Dew-point Pressure Deviation, %
50	34.82	1.4
10	32.23	2.9
4	27.89	9.2
2	21.74	22.4

Table 8. Deviation of high-pressure dew-point pressure of the Kelvin Equation. Deviation in the values of Dew-point pressure for predictions of the Kelvin Equation (Eq. 3) with that of the high-pressure Experimental Data (Figure 31)

Temperature, F	Kelvin Equation Pressure, psia	Experimental Data, psia	Dew-point Pressure Deviation, %
75	30.89	32.08	3.7
167.5	125.85	125.94	0.1
247.3	313.27	308.55	1.5

Hence, the results (as shown in Table 7 and Table 8 as wells as Figure 30 and Figure 31) show that predictions from the Kelvin Equation (Eq. 3) are consistent with the experimental data when the channel depth is 50 nm or higher (and the deviations are significant for values of channel depth less than 10 nm). This is consistent with the reports of Zhong et al. [95] showing similar behavior for deviations in the bubble-point temperature of propane in an 8 nm channel. They reported a maximum difference of 8% between the experimental data and the predictions from the Kelvin Equation (Eq. 3). For high-pressure experiments, since the channels used are 10 nm in depth, the predictions from the Kelvin Equation still provides a very close match in all temperature ranges.

Further effects of temperature on Kelvin Equation prediction is needed for smaller channels (4 and 2 nm) where Kelvin Equation starts to deviate. The significant deviation in pressure for channel sizes less than 10 nm can be attributed to non-continuum effects (i.e., the values of interfacial tension under bulk conditions may be significantly different compared to that of confined fluids).

The surface wettability can also alter fluid confinement effect (in other words, the wettability of the walls can significantly affect the physical properties of the confined fluid). For example, the channel walls for the experimental apparatus consist of silicon dioxide, which is water wet. In contrast, the walls of the nano-scale pores in shale usually consist of kerogens (which are typically non-wetting for water and wetting for hydrocarbons). However, as shown by molecular simulation results in the literature [45], surfaces made from quartz and kerogen demonstrate similar degrees of confinement effect on hydrocarbon phase behavior. This is because - quartz and kerogen having different values of effective contact angle values (i.e., wettability behavior) for water and hydrocarbons.

3.4 Measurement Uncertainty Analysis

The measurement uncertainty for the dew-point pressure of n-Butane consists of three parts. The first part is the inherent inaccuracy of the pressure gauge used in the experiment. The second part is the inherent inaccuracy of the IR camera used in the experiment. The third part is the result of human error during the experimental process. The pressure gauge used in this work is The BetaGauge PI PRO with an accuracy of 0.05%. The pressure transducer used in high-pressure setup (PX409-3.5KGUSBH, OMEGA Engineering, Inc) has an accuracy of 0.08%. The IR camera used has an accuracy rating of 2%. The human error during the experiment is overcome by

measuring each property three times to obtain the average values. The standard deviation of the three measurement values is calculated as the human error values. The final experimental uncertainty is the summation of equipment uncertainty and human error. The calculated experimental errors are listed below in Table 9 and 10 for low-pressure experiment and high-pressure experiment respectively. For the calculation of error from IR camera measurements, since the confined condensation pressure data is not sufficient enough to conclude a correlation between temperature and pressure, it is assumed that they have a linear relationship with a slope of 1. Therefore, an error of 2% from the temperature measurement will correlate to an error of 2% in pressure measurement.

Table 9. Measurement Uncertainties for room temperature experiment.

Depth, nm	Average Pressure Measurement, psi	Human Error, psi	Error from Pressure Gauge, psi	Error from IR Camera, psi	Total Error, psi
50	35.3	0.2	0.0	0.7	0.9
10	33.2	0.2	0.0	0.7	0.9
4	30.7	0.1	0.0	0.6	0.7
2	27.2	0.3	0.0	0.5	0.8

Table 10. Measurement Uncertainties for experiment with elevated temperature.

Temperature, °F	Average Pressure Measurement, psi	Human Error, psi	Error from Pressure Gauge, psi	Error from IR Camera, psi	Total Error, psi
75	32.08	0.14	0.02	0.64	0.76
167.5	125.94	0.42	0.06	2.52	2.98
247.3	308.55	0.65	0.15	6.17	6.92

3.5 Hysteresis Effect

In addition to the confined behavior noted in the previous section, additional peculiarities were observed in this study. For example, the hysteresis effect for the values of bubble point and dew-point pressure values are observed in these experiments, where the deviations are significantly higher for channel depths below 10 nm. These experiments were performed using n-Butane as the test fluid. The values of bubble point pressure and dew point pressure were measured experimentally for different values of channel depth in the same micro/nano-fluidic chips. The values of bubble point pressure (as well as dew point pressure) were observed to be significantly different when the pressure was progressively increased (from a minimum value chosen for these experiments) or progressively decreased (from a maximum value chosen for these experiments). The hysteresis effect can be quantified by obtaining the difference between the values of the dew-point pressure and bubble-point pressure (when the pressure is progressively increased or progressively decreased). The dew-point pressure is recorded when the first drop of liquid is observed under a microscope during the process steps involving a progressive increase in the values of pressure. The bubble-point pressure is recorded when the first gas bubble is observed under a microscope during the process steps involving a progressive decrease in the values of pressure.

In this study, the pressure is decreased at the rate of 0.2 psi/minute (which is also the same rate when the pressure is increased). Values listed in Table 11 demonstrate the variation in the hysteresis effect for different values of channel depth. Table 11 shows that for channel depths of 10 nm and 50 nm, the hysteresis effect is almost non-existent as the difference between the bubble point pressure and dew point pressure is less than 1 psi (for 50 nm) and 1.5 psi (for 10 nm). For

experiments involving channel depths of 50 nm, 10 nm and 4 nm, when the first bubble is formed

the liquid phase of n-Butane in the entire channel is evaporated in a few seconds (similarly during

condensation – the condensate covers the entire channel in a few seconds). However, for

experiments involving channel depth of 2 nm, even after the pressure is decreased to atmosphere

pressure, the entire channel is still occupied with liquid n-Butane. The evaporation of the test liquid

is not observed in these experiments (in contrast to the experiments involving channel depths of

50 nm, 10 nm and 4 nm where complete evaporation within the channels is observed for pressures

above ambient conditions), as shown in Figure 32.

This anomalous behavior is still not fully understood. Presumably, n-Butane confined in 2 nm

capillaries requires significantly longer time to reach equilibrium in comparison (in comparison to

that of the other larger capillaries) and the rate of change pressure imposed during the experiments

(which is 0.2 psi/ minute) may be too fast for the constraints involving channel depth of 2 nm.

Hence additional experiments need to be performed (especially for channel depths ranging from

2-4 nm in steps of 1 nm) for quantifying the hysteresis effect as a function of different experimental

conditions (e.g., rate of change of pressure).

Table 11. Hysteresis effect for different values of channel depth.

Depth, nm	Dew-point pressure, psia	Bubble-point pressure, psia	Hysteresis, psi
50	35.3	34.4	0.9
10	33.2	31.8	1.4
4	30.7	29.6	1.1
2	27.2	<14.7	>12.5
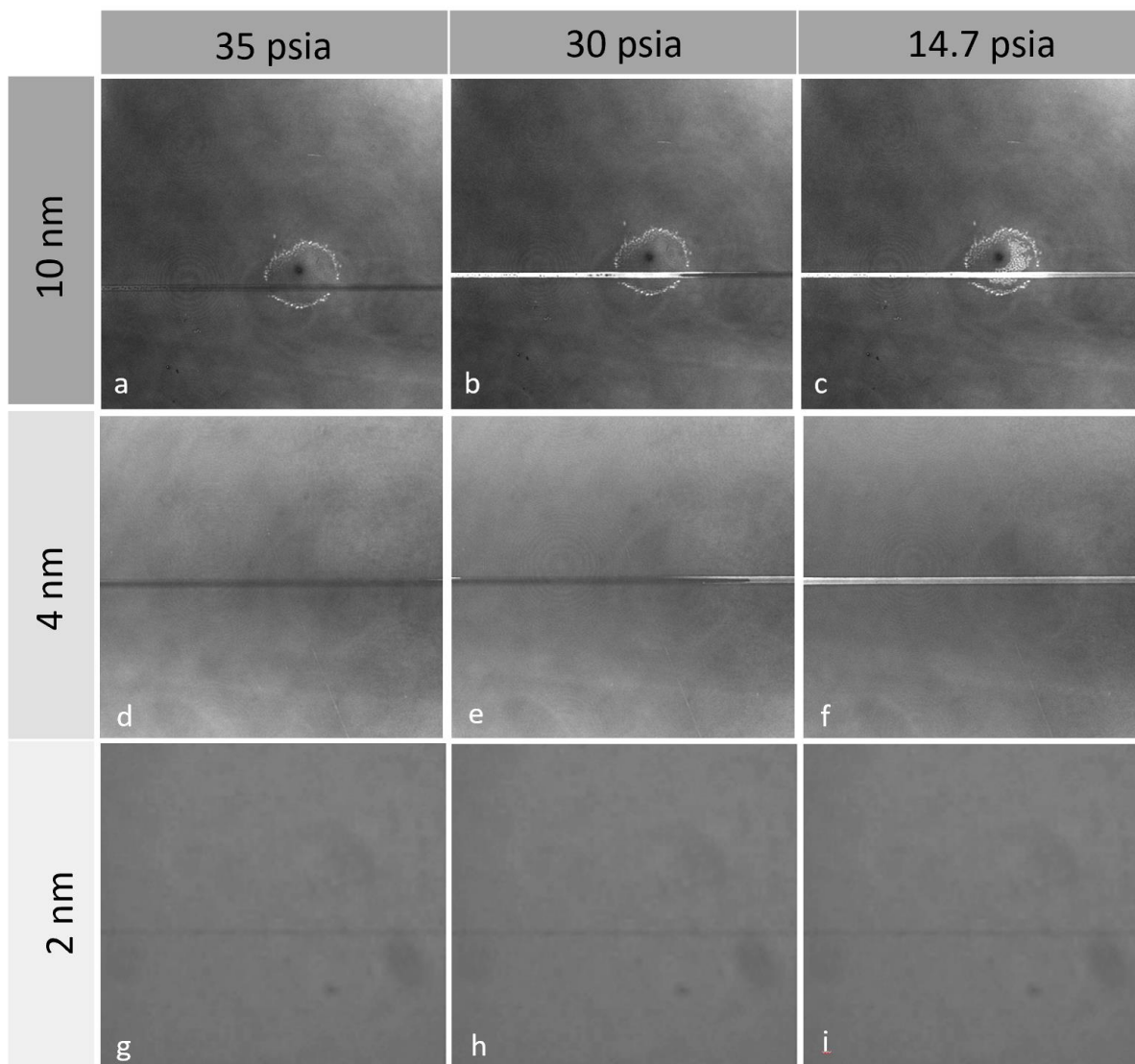
Figure 32. Vaporization process of n-Butane in different channels. Sequence of images showing the evaporation process of n-Butane in different channels (with channel depths of 2 nm, 4 nm and 10 nm). (a, d, g) the channels are initially occupied with liquid n-Butane. (b, e) liquid n-Butane starts to evaporate as the pressure decreases. (c, f) liquid n-Butane is evaporated everywhere inside the channel. (h, i) liquid n-Butane is not evaporated in the 2 nm channel even if the pressure is dropped to atmospheric pressure.

4. SUMMARY AND FUTURE WORK

Material properties and thermodynamic behavior of hydrocarbons display anomalous and significant deviations when restricted to miniaturized containers (i.e., small volume of the fluids in confined spaces) — in comparison to that of the bulk quantities of the same fluids (i.e., bulk properties). This is caused by the increasingly dominant fluid–wall interactions, rather than conventionally dominant fluid–fluid interactions in the bulk. This new fluid–wall interaction causes fluid molecules to distribute nonuniformly inside the confined space, thus altering fluid behavior and thermo-physical properties. This is the so-called confinement effect.

One of the effects of this confinement is the alteration of fluid-phase behavior. The characterization of fluid-phase behavior is crucial in the shale oil and gas industry since it has a direct impact on production-optimization and ultimate oil recovery. Pore-size distribution studies on shale rock have shown that a large proportion of shale rock consists of nanoscale pores. Therefore, correctly characterizing hydrocarbon phase behavior in shale rock requires a well-rounded understanding of the physics of the confinement effect. Many attempts have been made to better understand the confinement effect in the shale matrix, including molecular simulations and experimentation. The simulation techniques applied include molecular simulation, density functional theory, and equations of state. However, there is a paucity of experimental work that has been conducted in this field (especially experiments with sub-10 nm capillaries). Therefore, the simulations performed do not have a reliable set of experimental data for proper validation.

In this study, an experimental technology (lab-on-a-chip) was implemented. This technology is used in a large variety of research topics (such as chemistry, life sciences, etc.) and has been widely adapted for commercial applications as well. The lab-on-a-chip technology utilizes nanofluidic or microfluidic devices containing nanoscale capillaries as small as 2 nm. In the study of fluid-phase behavior, this technology has many advantages, including small sample requirements, flexible device patterns, simple experimental setup, flexibility in design, and ease for experimental visualization. Owing to the nature of this technology, it has great potential for future experimentation in the shale oil and gas industry — in addition to the study of deviations in the hydrocarbon phase behavior that was explored in this study.

In Chapter 2, the design and fabrication of nanofluidic devices were described. The fabrication process for nanofluidic devices is a standard process that was adapted from other fields of study, (with proper optimization of the recipes to suit the requirements of the experiments). A trade-off needs to be evaluated in regard to the pressure tolerance of the device, the size of the features etched, the visualization limit, and the success rate of the fabrication. Selection of an optimized set of parameters is crucial for both fulfilling the experimental requirements and maximizing the fabrication yield. After presenting the fabrication steps, the two experimental setups used in this study were discussed. The low-pressure setup, capable of handling sub-100 psi environments, is assembled and tested initially as a means for validating the experimental methodology and for generating results for low-pressure conditions. The low-pressure setup includes a hand pump, vacuum syringe, hydrocarbon source, microscope, pressure gauge, and an IR camera as the primary equipment. After successfully testing the low-pressure setup, a high-pressure setup was fabricated and assembled to perform the desired experiments in a high-temperature, high-pressure

environment that more closely resembles the conditions within shale reservoirs. The high-pressure setup includes an ISCO pump, a vacuum pump, a water-cooling system, a heating system, a microscope, pressure transducers, and an IR camera. Furthermore, instead of using plastic tubing like in the low-pressure experimental setup, stainless-steel tubing was used in the high-pressure setup. This high-pressure setup allows testing at a significantly higher pressure (7000 psi) and facilitates better fluid control. The experimental procedure was optimized prior to establishing the final experimental protocol. One of the main issues during experimentation was the presence of the gas impurities; which can be mitigated by eliminating the air inside the tubing prior to experiments and by using a longer flush time for the hydrocarbons inside the nanofluidic device. The pictures obtained from the flow visualization experiments clearly show the hydrocarbon condensation and vaporization processes that were achieved during the experiments. The data recorded from the pressure gauges was used to demonstrate and validate the predictions for the confinement effect during the phase transition processes.

In Chapter 3, the experimental results are presented and compared with the predictions from different models. From the experimental results, it can be concluded that the confinement effect for hydrocarbons in nanoscale pores becomes significant when the channel depth is lower than 10 nm. The confinement effect above 10 nm is not significant. The confinement effect—especially for 2-nm and 4-nm channels— is perceptible significantly, with a 23.3% decrease in dew-point pressure of n-butane in the 2-nm channel. Further, the high-pressure experiments demonstrated that the confinement effect—for a constant channel depth—tended to decrease as the temperature increased.

The experimental data was compared with the predictions from the simulation models using the Kelvin equation, molecular simulations, and altered equations of state. When using the Kelvin equation, the predicted pressures match well with the experimental data for channel sizes of 10 nm and above. However, as the channel size decreases to 4 nm and 2 nm, the Kelvin equation predictions for pressure deviates from the experimental value by 9.2% and 22.4% respectively. This indicates that the Kelvin equation does not provide adequate approximations when the capillary size is extremely small. In the high-temperature and high-pressure experiments — for a constant capillary size—the Kelvin Equation tends to provide more consistent predictions when the temperature of the environment is high. The comparison between the equation of state with added capillary pressure and the experimental data shows that the altered equation of state model is not currently a very precise tool for use, as it greatly underestimated the dew-point pressure for n-butane in 10-nm channels. In contrast, the molecular simulation results also demonstrated a promising match to the experimental dew-point pressure data for all channel sizes.

During the experiments, an abnormally strong hysteresis effect was observed for 2-nm channels. The hysteresis was measured by calculating the difference between the dew-point pressure (while the pressure increased) and the bubble-point pressure (while the pressure decreased). For channels with a depth of 4-nm, 10-nm, and 50-nm: the hysteresis effect was not very strong — since there was approximately a 1 psi difference between the two pressure measurements. However, for the 2-nm channel, the hysteresis effect was extremely strong. Once condensation occurred inside the 2-nm channel, liquid n-butane could not be evaporated even if the pressure was decreased to atmospheric pressure. This means that the hysteresis effect for 2-nm channels is greater than 12.5 psi at the very least.

Molecular simulations have also been conducted to model the hysteresis effect; however, the model obtains a vaporization pressure of 16 psi, which is slightly above atmospheric pressure. The reason for this strong hysteresis is not fully understood and requires further investigation. One possible explanation, though, is that the 2-nm channel requires a much greater time interval for the system to achieve equilibrium conditions in each step, i.e., for pressure-increasing or pressure-decreasing steps. The rate of pressure change used in larger channels may not be slow enough for the 2-nm channel; this creates a non-equilibrium system and the strong hysteresis effect.

Although significant progress has been made by applying the lab-on-a-chip technology to the study of shale rock systems, much more work can be performed to improve the experimental process and its applications. There are several future directions for work in this field. First, the pressure capacity of the device and the experimental setup should be increased. As mentioned in previous chapters, the pressure tolerance of the experimental setup is 7500 psi; however, the pressure tolerance of current devices is around 1000 psi. Even though significant improvements have been made for improving the pressure tolerance of the device, its current pressure tolerance is as high as reservoir pressures, which are usually of the order of several thousand psi.

Second, a more realistic feature design is required, which can mimic rock micro- and nano-structures. Finally, only n-butane has been used as the fluid to study the confinement effect in this research. Measurements of other chemicals — such as propane, pentane, and heptane—should be conducted to generate a comprehensive dataset for simulation models, in order to validate their results. Once these single-component measurements are complete, the measurements of mixtures

of several components (for example, a mixture of methane, n-butane, and heptane) can be conducted to further investigate the confinement effect on fluid-phase behavior.

REFERENCES

1. Clarkson, C.R., et al., *Pore structure characterization of North American shale gas reservoirs using USANS/SANS, gas adsorption, and mercury intrusion.* Fuel, 2013. **103**: p. 606-616.

2. Kuila, U. and M. Prasad, *Specific surface area and pore-size distribution in clays and shales.* Geophysical Prospecting, 2013. **61**(2): p. 341-362.

3. Labani, M.M., et al., *Evaluation of pore size spectrum of gas shale reservoirs using low pressure nitrogen adsorption, gas expansion and mercury porosimetry: A case study from the Perth and Canning Basins, Western Australia.* Journal of Petroleum Science and Engineering, 2013. **112**: p. 7-16.

4. Ross, D.J. and R.M. Bustin, *The importance of shale composition and pore structure upon gas storage potential of shale gas reservoirs.* Marine and Petroleum Geology, 2009. **26**(6): p. 916-927.

5. Strapoc, D., et al., *Geochemical constraints on the origin and volume of gas in the New Albany Shale (Devonian–Mississippian), eastern Illinois Basin.* AAPG bulletin, 2010. **94**(11): p. 1713-1740.

6. Chalmers, G.R. and R.M. Bustin, *The organic matter distribution and methane capacity of the Lower Cretaceous strata of Northeastern British Columbia, Canada.* International Journal of Coal Geology, 2007. **70**(1-3): p. 223-239.

7.   Chalmers, G.R., R.M. Bustin, and I.M. Power, *Characterization of gas shale pore systems by porosimetry, pycnometry, surface area, and field emission scanning electron microscopy/transmission electron microscopy image analyses: Examples from the Barnett, Woodford, Haynesville, Marcellus, and Doig units.* AAPG Bulletin, 2012. **96**(6): p. 1099-1119.

8.   Curtis, M.E., et al. *Transmission and scanning electron microscopy investigation of pore connectivity of gas shales on the nanoscale*. in *North American unconventional gas conference and exhibition*. 2011. Society of Petroleum Engineers.

9.   Curtis, M.E., C.H. Sondergeld, and C.S. Rai. *Investigation of the microstructure of shales in the oil window*. in *Unconventional Resources Technology Conference*. 2013. Society of Exploration Geophysicists, American Association of Petroleum Geologists, Society of Petroleum Engineers.

10.   Sigal, R.F., *Pore-Size Distributions for Organic-Shale-Reservoir Rocks From Nuclear-Magnetic-Resonance Spectra Combined With Adsorption Measurements.* SPE Journal, 2015. **20**(04).

11.   Gay, J., J. Suzanne, and J.J.P.R.B. Coulomb, *Wetting, surface melting, and freezing of thin films of methane adsorbed on MgO (100).* 1990. **41**(16): p. 11346.

12.   Madih, K., et al., *Thin methane film growing mode on MgO/100 surface.* 1989. **8**(5): p. 459.

13.   Franck, C., *Fundamentals of Inhomogeneous Fluids ed D Henderson*. 1992, New York: Dekker.

14.   Fluid, I.P., *Fluid Interfacial Phenomena*. 1986, John Wiley & Sons.

15.   Beamish, J., et al., *Solidification and Superfluidity of He 4 in Porous Vycor Glass.* 1983. **50**(6): p. 425.

16.   Gubbins, K.E., M. Sliwinska-Bartkowiak, and S.-H.J.M.S. Suh, *Molecular Simulations of Phase Transitions in Pores.* 1996. **17**(4-6): p. 333-367.

17.   Nelson, D., *Bond-orientational order in condensed matter systems*. 2012: Springer Science & Business Media.

18.   Angelova, A., et al., *Dynamic control of nanofluidic channels in protein drug delivery vehicles.* Journal of Drug Delivery Science and Technology, 2008. **18**(1): p. 41-45.

19.   Zeng, Y. and D.J. Harrison, *Self-assembled colloidal arrays as three-dimensional nanofluidic sieves for separation of biomolecules on microchips.* Analytical chemistry, 2007. **79**(6): p. 2289-2295.

20.   Benedetti, L., et al., *Light-activated protein interaction with high spatial subcellular confinement.* 2018. **115**(10): p. E2238-E2245.

21.   Chow, E. and J.J.P.o.t.N.A.o.S. Skolnick, *Effects of confinement on models of intracellular macromolecular dynamics.* 2015. **112**(48): p. 14846-14851.

22.   Sharma, S. and P.G.J.P.o.t.N.A.o.S. Debenedetti, *Evaporation rate of water in hydrophobic confinement.* 2012. **109**(12): p. 4365-4370.

23.   Kim, S.J., et al., *Direct seawater desalination by ion concentration polarization.* Nature Nanotechnology, 2010. **5**(4): p. 297.

24.   Yang, H.Y., et al., *Carbon nanotube membranes with ultrahigh specific adsorption capacity for water desalination and purification.* Nature communications, 2013. **4**: p. 2220.

25.   Jin, Z. and A. Firoozabadi, *Thermodynamic Modeling of Phase Behavior in Shale Media.* 2016.

26.   Singh, S.K., et al., *Vapor− liquid phase coexistence, critical properties, and surface tension of confined alkanes.* The Journal of Physical Chemistry C, 2009. **113**(17): p. 7170-7180.

27.   Luo, S., J.L. Lutkenhaus, and H. Nasrabadi. *Effect of Nano-Scale Pore Size Distribution on Fluid Phase Behavior of Gas IOR in Shale Reservoirs.* in *SPE Improved Oil Recovery Conference.* 2018. Society of Petroleum Engineers.

28.   Alharthy, N., et al., *Enhanced oil recovery in liquid-rich shale reservoirs: laboratory to field.* SPE Reservoir Evaluation & Engineering, 2017.

29.   Nojabaei, B., R.T. Johns, and L. Chu, *Effect of capillary pressure on phase behavior in tight rocks and shales.* SPE Reservoir Evaluation & Engineering, 2013. **16**(03): p. 281-289.

30.   Stimpson, B.C. and M.A. Barrufet. *Effects of Confined Space on Production from Tight Reservoirs*. in *SPE Annual Technical Conference and Exhibition*. 2016. Society of Petroleum Engineers.

31.   Jin, Z. and A. Firoozabadi, *Thermodynamic modeling of phase behavior in shale media.* SPE Journal, 2016. **21**(01): p. 190-207.

32.   Teklu, T.W., et al., *Phase Behavior and Minimum Miscibility Pressure in Nanopores.* SPE Reservoir Evaluation & Engineering, 2014.

33.   Ma, Y., L. Jin, and A. Jamili. *Modifying van der Waals equation of state to consider influence of confinement on phase behavior*. in *SPE Annual Technical Conference and Exhibition*. 2013. Society of Petroleum Engineers.

34.   Stimpson, B.C. and M.A. Barrufet, *Thermodynamic modeling of pure components including the effects of capillarity.* Journal of Chemical & Engineering Data, 2016. **61**(8): p. 2844-2850.

35.   Firoozabadi, A., *Thermodynamics and Applications of Hydrocarbons Energy Production*. 2015: McGraw-Hill Education.

36.   Sapmanee, K., *Effects of pore proximity on behavior and production prediction of gas/condensate*. 2011, University of Oklahoma.

37.   Jin, L., Y. Ma, and A. Jamili. *Investigating the effect of pore proximity on phase behavior and fluid properties in shale formations*. in *SPE Annual Technical Conference and Exhibition*. 2013. Society of Petroleum Engineers.

38.   Devegowda, D., et al. *Phase behavior of gas condensates in shales due to pore proximity effects: Implications for transport, reserves and well productivity*. in *SPE annual technical conference and exhibition*. 2012. Society of Petroleum Engineers.

39.   Alharthy, N.S., et al. *Multiphase compositional modeling in small-scale pores of unconventional shale reservoirs*. in *SPE Annual Technical Conference and Exhibition*. 2013. Society of Petroleum Engineers.

40.   Li, Z., Z. Jin, and A. Firoozabadi, *Phase Behavior and Adsorption of Pure Substances and Mixtures and Characterization in Nanopore Structures by Density Functional Theory.* SPE Journal, 2014. **19**(06).

41.   Liu, Y., Z. Jin, and H.A. Li, *Comparison of Peng-Robinson Equation of State With Capillary Pressure Model With Engineering Density-Functional Theory in Describing the Phase Behavior of Confined Hydrocarbons.* SPE Journal, 2018.

42.   Pitakbunkate, T., et al., *Effect of Confinement on Pressure/Volume/Temperature Properties of Hydrocarbons in Shale Reservoirs.* SPE Journal, 2016. **21**(02).

43.   Didar, B.R. and I.Y. Akkutlu, *Pore-size Dependence of Fluid Phase Behavior and Properties in Organic-Rich Shale Reservoirs*, in *SPE International Symposium on Oilfield Chemistry*. 2013, Society of Petroleum Engineers.

44.   Psarras, P., et al., *Methane and CO2 adsorption capacities of kerogen in the Eagle Ford shale from molecular simulation.* Accounts of chemical research, 2017. **50**(8): p. 1818-1828.

45.   Jin, B. and H. Nasrabadi, *Phase Behavior in Shale Organic/Inorganic Nanopores From Molecular Simulation.* 2018.

46.   Jin, B. and H. Nasrabadi, *Phase behavior of multi-component hydrocarbon systems in nano-pores using gauge-GCMC molecular simulation.* Fluid Phase Equilibria, 2016. **425**: p. 324-334.

47.   Jin, B., R. Bi, and H. Nasrabadi, *Molecular simulation of the pore size distribution effect on phase behavior of methane confined in nanopores.* Fluid Phase Equilibria, 2017. **452**(Supplement C): p. 94-102.

48.   Bi, R. and H. Nasrabadi, *Molecular simulation of the constant composition expansion experiment in shale multi-scale systems.* Fluid Phase Equilibria, 2019. **495**: p. 59-68.

49.   Vishnyakov, A. and A.V.J.T.J.o.P.C.B. Neimark, *Studies of Liquid− Vapor Equilibria, Criticality, and Spinodal Transitions in Nanopores by the Gauge Cell Monte Carlo Simulation Method.* 2001. **105**(29): p. 7009-7020.

50.   Bao, B., et al., *Microfluidic and nanofluidic phase behavior characterization for industrial CO2, oil and gas.* Lab on a Chip, 2017.

51.   McKeogh, G., *Moisture Measurement Technologies for Natural Gas.* GE Measurement & Control, 2000.

52.   Potter, D. and A.P. Instruments, *Analytical devices for the measurement of water vapor in the natural gas process and transmission industry.* GAS2011, Rotterdam, 2011.

53.   Wu, W., J. Ke, and M. Poliakoff, *New design of fiber-optic reflectometer for determining the phase boundary of multicomponent fluid mixtures at high pressures and high temperatures.* Review of scientific instruments, 2006. **77**(2): p. 023903.

54.   Bao, B., H. Fadaei, and D. Sinton, *Detection of bubble and dew point using optical thin-film interference.* Sensors and Actuators B: Chemical, 2015. **207**: p. 640-649.

55.   Luo, S., J.L. Lutkenhaus, and H. Nasrabadi, *Use of Differential Scanning Calorimetry to Study Phase Behavior of Hydrocarbon Mixtures in Nano-Scale Porous Media.* Journal of Petroleum Science and Engineering, 2016.

56.   Luo, S., J.L. Lutkenhaus, and H. Nasrabadi, *Experimental Study of Confinement Effect on Hydrocarbon Phase Behavior in Nano-Scale Porous Media Using Differential Scanning Calorimetry*, in *SPE Annual Technical Conference and Exhibition*. 2015, Society of Petroleum Engineers: Houston, Texas, USA.

57.   Luo, S., H. Nasrabadi, and J.L. Lutkenhaus, *Effect of confinement on the bubble points of hydrocarbons in nanoporous media.* AIChE Journal, 2016.

58.   Luo, S., et al., *A novel pore-size-dependent equation of state for modeling fluid phase behavior in nanopores.* Fluid Phase Equilibria, 2019. **498**: p. 72-85.

59.   Salahshoor, S. and M. Fahes. *Experimental Investigation of the Effect of Pore Size on Saturation Pressure for Gas Mixtures*. in *SPE Annual Technical Conference and Exhibition*. 2018. Society of Petroleum Engineers.

60.   Kim, B., et al., *Purification of high salinity brine by multi-stage ion concentration polarization desalination.* Scientific reports, 2016. **6**: p. 31850.

61.   MacDonald, B.D., et al., *Out-of-plane ion concentration polarization for scalable water desalination.* Lab on a Chip, 2014. **14**(4): p. 681-685.

62.   Vladisavljević, G.T., et al., *Industrial lab-on-a-chip: design, applications and scale-up for drug discovery and delivery.* Advanced drug delivery reviews, 2013. **65**(11-12): p. 1626-1663.

63.   Weigl, B.H., R.L. Bardell, and C.R. Cabrera, *Lab-on-a-chip for drug development.* Advanced drug delivery reviews, 2003. **55**(3): p. 349-377.

64.   Santini, J., John T, et al., *Microchips as controlled drug-delivery devices.* Angewandte Chemie International Edition, 2000. **39**(14): p. 2396-2407.

65.   Dittrich, P.S. and A. Manz, *Lab-on-a-chip: microfluidics in drug discovery.* Nature reviews Drug discovery, 2006. **5**(3): p. 210.

66.   Manz, A., et al., *Electroosmotic pumping and electrophoretic separations for miniaturized chemical analysis systems.* Journal of Micromechanics and Microengineering, 1994. **4**(4): p. 257.

67.   Harrison, D.J., et al., *Micromachining a miniaturized capillary electrophoresis-based chemical analysis system on a chip.* Science, 1993. **261**(5123): p. 895-897.

68.   Li, P.C., *Microfluidic lab-on-a-chip for chemical and biological analysis and discovery*. 2005: CRC press.

69.   Mostowfi, F., S. Molla, and P. Tabeling, *Determining phase diagrams of gas–liquid systems using a microfluidic PVT.* Lab on a Chip, 2012. **12**(21): p. 4381-4387.

70.   Fisher, R., et al., *Equilibrium gas–oil ratio measurements using a microfluidic technique.* Lab on a Chip, 2013. **13**(13): p. 2623-2633.

71.   Pinho, B., et al., *A microfluidic approach for investigating multicomponent system thermodynamics at high pressures and temperatures.* Lab on a Chip, 2014. **14**(19): p. 3843-3849.

72.   Bao, B., et al., *Direct Measurement of the Fluid Phase Diagram.* Analytical Chemistry, 2016. **88**(14): p. 6986-6989.

73.   Song, W., H. Fadaei, and D. Sinton, *Determination of dew point conditions for CO2 with impurities using microfluidics.* Environmental science & technology, 2014. **48**(6): p. 3567-3574.

74.   Togo, M., et al., *Measurement and correlation of phase equilibria for (water+ aromatic hydrocarbon) binary mixtures at T=(573 to 623) K using microfluidic mixing.* The Journal of Chemical Thermodynamics, 2013. **67**: p. 247-252.

75.   Luther, S.K., et al., *Determination of Vapor–Liquid Equilibrium Data in Microfluidic Segmented Flows at Elevated Pressures Using Raman Spectroscopy.* Analytical chemistry, 2015. **87**(16): p. 8165-8172.

76.   Sullivan, M.T. and D.E. Angelescu, *Microfluidic Bubble Point Measurement Using Thermal Nucleation.* Energy & Fuels, 2016. **30**(4): p. 2655-2661.

77.   Abolhasani, M., et al., *Automated microfluidic platform for studies of carbon dioxide dissolution and solubility in physical solvents.* Lab on a Chip, 2012. **12**(9): p. 1611-1618.

78.   Lefortier, S.G., et al., *Rapid microfluidic screening of CO 2 solubility and diffusion in pure and mixed solvents.* Lab on a Chip, 2012. **12**(18): p. 3387-3391.

79.   Liu, N., et al., *Microfluidic approach for studying CO2 solubility in water and brine using confocal Raman spectroscopy.* Chemical Physics Letters, 2012. **551**: p. 139-143.

80.   Luther, S.K., et al., *Microfluidic investigation into mass transfer in compressible multi-phase systems composed of oil, water and carbon dioxide at elevated pressure.* The Journal of Supercritical Fluids, 2013. **84**: p. 121-131.

81.   Lin, Y., et al., *Measurement of temperature-dependent diffusion coefficients using a confocal Raman microscope with microfluidic chips considering laser-induced heating effect.* Analytica chimica acta, 2010. **667**(1-2): p. 103-112.

82.   Fadaei, H., B. Scarff, and D. Sinton, *Rapid microfluidics-based measurement of CO2 diffusivity in bitumen.* Energy & Fuels, 2011. **25**(10): p. 4829-4835.

83.   Fadaei, H., J.M. Shaw, and D. Sinton, *Bitumen–toluene mutual diffusion coefficients using microfluidics.* Energy & Fuels, 2013. **27**(4): p. 2042-2048.

84.   Sell, A., et al., *Measurement of CO2 diffusivity for carbon sequestration: A microfluidic approach for reservoir-specific analysis.* Environmental science & technology, 2013. **47**(1): p. 71-78.

85.   Nguyen, P., et al., *Fast fluorescence-based microfluidic method for measuring minimum miscibility pressure of CO2 in crude oils.* Analytical chemistry, 2015. **87**(6): p. 3160-3164.

86.   Bowden, S.A., et al., *Determination of the asphaltene and carboxylic acid content of a heavy oil using a microfluidic device.* Lab on a Chip, 2009. **9**(6): p. 828-832.

87.   Sieben, V.J., et al., *Asphaltenes yield curve measurements on a microfluidic platform.* Lab on a Chip, 2015. **15**(20): p. 4062-4074.

88.   Sieben, V.J., et al., *Microfluidic approach for evaluating the solubility of crude oil asphaltenes.* Energy & fuels, 2016. **30**(3): p. 1933-1946.

89.   Hu, C., J.E. Morris, and R.L. Hartman, *Microfluidic investigation of the deposition of asphaltenes in porous media.* Lab on a Chip, 2014. **14**(12).

90.   Molla, S., L. Magro, and F. Mostowfi, *Microfluidic technique for measuring wax appearance temperature of reservoir fluids.* Lab on a Chip, 2016. **16**(19): p. 3795-3803.

91.   Duan, C. and A. Majumdar, *Anomalous ion transport in 2-nm hydrophilic nanochannels.* Nat Nano, 2010. **5**(12): p. 848-852.

92.   Wang, L., et al., *Experimental Study and Modeling of the Effect of Nanoconfinement on Hydrocarbon Phase Behavior in Unconventional Reservoirs*, in *SPE Western North American and Rocky Mountain Joint Meeting*. 2014, Society of Petroleum Engineers: Denver, Colorado.

93.   Parsa, E., X. Yin, and E. Ozkan, *Direct Observation of the Impact of Nanopore Confinement on Petroleum Gas Condensation*, in *SPE Annual Technical Conference and Exhibition*. 2015, Society of Petroleum Engineers: Houston, Texas, USA.

94.   Alfi, M., H. Nasrabadi, and D. Banerjee, *Experimental investigation of confinement effect on phase behavior of hexane, heptane and octane using lab-on-a-chip technology.* Fluid Phase Equilibria, 2016. **423**: p. 25-33.

95.   Zhong, J., et al., *Capillary Condensation in 8 nm Deep Channels.* The Journal of Physical Chemistry Letters, 2018. **9**(3): p. 497-503.

96.   Zhong, J., et al., *Condensation in One-Dimensional Dead-End Nanochannels.* ACS nano, 2016. **11**(1): p. 304-313.

97.   Xu, Y., et al., *The Full Pressure–Temperature Phase Envelope of a Mixture in 1000 Microfluidic Chambers.* Angewandte Chemie International Edition, 2017. **56**(45): p. 13962-13967.

98.   Yang, Q., et al., *Direct visualization and molecular simulation of dewpoint pressure of a confined fluid in sub-10 nm slit pores.* Fuel, 2019. **235**: p. 1216-1223.

99.   Alfi, M., H. Nasrabadi, and D. Banerjee. *Confinement effects on phase behavior of hydrocarbon in nanochannels*. in *ASME 2015 International Mechanical Engineering Congress and Exposition*. 2015. American Society of Mechanical Engineers Digital Collection.

100. Dziuban, J.A., *Bonding in microsystem technology*. Vol. 24. 2007: Springer Science & Business Media.

101. Grumezescu, A., *Nanobiomaterials in hard tissue engineering: applications of nanobiomaterials*. 2016: William Andrew.

102. Lima, M., V. Correlo, and R. Reis, *Micro/nano replication and 3D assembling techniques for scaffold fabrication.* Materials Science and Engineering: C, 2014. **42**: p. 615-621.

103. McCord, M.A. and M.J. Rooks. *SPIE handbook of microlithography, micromachining and microfabrication*. in *SPIE, Bellingham*. 2000.

104. Kumar, P., et al., *Effect of HF concentration on physical and electronic properties of electrochemically formed nanoporous silicon.* Journal of Nanomaterials, 2009. **2009**.

105. Zhang, X., S. Collins, and R. Smith, *Porous silicon formation and electropolishing of silicon by anodic polarization in HF solution.* Journal of the electrochemical society, 1989. **136**(5): p. 1561.

106. Herino, R., et al., *Porosity and pore size distributions of porous silicon layers.* Journal of the electrochemical society, 1987. **134**(8): p. 1994.

107. Shen, V., et al., *NIST standard reference simulation website, NIST standard reference database number 173.* National Institute of Standards and Technology, Gaithersburg MD, 2015. **20899**.